



1 **Evaluation of aerosol optical depths and clear-sky radiative fluxes of the**  
2 **CERES Edition 4.1 SYN1deg data product**

3

4

5 David W. Fillmore<sup>1</sup>, David A. Rutan<sup>2</sup>, Seiji Kato<sup>3</sup>, Fred G. Rose<sup>2</sup>,  
6 and Thomas E. Caldwell<sup>2</sup>

7

8 <sup>1</sup>University Center for Atmospheric Research, Boulder, CO. 80307

9

<sup>2</sup>SSAI, Hampton, VA, 23666

10

<sup>3</sup>NASA Langley Research Center, Hampton, VA, 23666

11

12

13

14

15

16

17

18

19

20

21

---

22 *Corresponding author address:* David W Fillmore,  
23 University Center for Atmospheric Research  
24 P.O. Box 3000  
25 Boulder, CO 80307  
26 E-mail: david.w.fillmore@ucar.edu



27 Abstract

28 Aerosol optical depths (AOD) used for the Edition 4.1 Clouds and the Earth's Radiant  
29 Energy System (CERES) Synoptic (SYN1deg) are evaluated. AODs are derived from  
30 Moderate Resolution Imaging Spectroradiometer (MODIS) observations and assimilated  
31 by an aerosol transport model (MATCH). As a consequence, clear-sky AODs closely  
32 match with those derived from MODIS instruments. AODs under all-sky conditions are  
33 larger than AODs under clear-sky conditions, which is supported by ground-based  
34 AERONET observations. When all-sky MATCH AODs are compared with Modern-Era  
35 Retrospective Analysis for Research and Applications (MERRA2) AODs, MATCH  
36 AODs are generally larger than MERRA2 AODS especially over convective regions (e.g.  
37 Amazon, central Africa, and eastern Asia). The difference is largely caused by MODIS  
38 AODs used for assimilation. Including AODs with larger retrieval uncertainty makes  
39 AODs over the convective regions larger. When AODs are used for clear-sky irradiance  
40 computations and computed downward shortwave irradiances are compared with ground-  
41 based observations, the computed instantaneous irradiances are 1% to 2% larger than  
42 observed irradiances. The comparison of top-of-atmosphere clear-sky irradiances with  
43 those derived from CERES observations suggests that AODs used for surface radiation  
44 observation sites are larger by 0.01 to 0.03, which is within the uncertainty of  
45 instantaneous MODIS AODs. However, the comparison with AERONET AOD suggests  
46 AODs used for computations over desert sites are 0.08 larger. The cause of positive  
47 biases of downward shortwave irradiance and AODs for the desert sites are unknown.  
48  
49



50        **1. Introduction**

51            Accurate estimates of the radiative effects of clouds and aerosols are essential for  
52 an understanding the radiative forcing to the Earth's climate system (Bauer and Menon,  
53 2012, Boucher et al. 2013). In addition, through the reflection and absorption of solar  
54 radiation, and the absorption and emission of terrestrial thermal radiation, clouds and  
55 aerosols affect the radiative heating of both the atmosphere and the surface, which in turn  
56 governs the atmospheric circulation and the hydrological cycle (e.g. Stephens et al. 2020,  
57 L'Ecuyer et al. 2015). Under the Earth Observing System (EOS) program, the National  
58 Aeronautics and Space Administration (NASA) has placed into orbit a series of satellites  
59 devoted to long term observations of the climate state. Among these are Terra and Aqua,  
60 the flagship satellites of the EOS. Central to observation of climate evolution are  
61 Moderate Resolution Imaging Spectroradiometer (MODIS) and the Clouds and the  
62 Earth's Radiant Energy System (CERES) instrument pairs that fly on both the Terra  
63 (March 2000 - present) and the Aqua (July 2002 - present) platforms (Wielicki et al.  
64 1996). Additional CERES instruments were launched (October 2011) upon the Suomi  
65 National Polar-orbiting Partnership (NPP) satellite along with the MODIS successor, the  
66 Visible Infrared Imager Radiometer Suite (VIIRS), and on the NOAA-20 satellite  
67 (November 2017). In addition to observations from these satellites, the CERES mission  
68 also integrates observations from the Geostationary Operational Environmental Satellites  
69 (GOES) (West and East), as well as other geostationary satellites around the globe, for  
70 full diurnal coverage of clouds and radiation.

71            The CERES instruments measure broadband radiances over the solar spectrum  
72 (shortwave), the thermal infrared (longwave radiance is obtained from a total channel



73 minus the shortwave channel), and the near infrared atmospheric window, with frequent  
74 on-board calibration. CERES measurements, in conjunction with MODIS information,  
75 are used to infer broadband irradiances through empirical angular distribution models  
76 (ADMs). Geosynchronous satellite imagery observes the diurnal cycle of clouds, which is  
77 not fully sampled by the polar orbiting satellites upon which CERES and MODIS reside.

78 While top-of-atmosphere (TOA) irradiances are derived from broadband  
79 radiances measured by CERES instruments (Loeb et al. 2005; Su et al. 2015), surface and  
80 in atmosphere irradiances are computed with a radiative transfer model. Inputs used for  
81 the computations include cloud properties derived from MODIS and geostationary  
82 satellites, aerosol optical depth derived from MODIS radiances, and surface albedo  
83 derived from MODIS and CERES observations (Rutan et al. 2009). Temperature and  
84 humidity profiles are provided by a reanalysis product produced by the NASA Goddard  
85 Modeling and Assimilation Office (GMAO).

86 Irradiances at the surface produced by the CERES team have been compared with  
87 surface observations (Rutan et al. 2015; Kato et al. 2013, 2018). These comparisons are  
88 for all-sky conditions (i.e. including any clouds). Irradiances under clear-sky conditions  
89 are not explicitly separated from all-sky conditions in the evaluations. There are several  
90 reasons that impede efforts at rigorous validation of clear-sky irradiances with surface  
91 observations; 1) a clear-sky condition at a given site does not persist over a long time  
92 (e.g. a month or longer), 2) there are mismatches of clear-sky conditions determined by  
93 satellite- and ground-based instruments, and 3) field-of-view size between CERES  
94 instruments and ground-based radiometers differ.



95           Despite these difficulties for evaluating computed clear-sky irradiances, clear-sky  
96 irradiances play an important role in quantifying aerosol and cloud radiative effects (Loeb  
97 and Su 2010; Soden and Chung 2017). Therefore, the uncertainty in surface irradiances  
98 need to be understood in order to assess the uncertainty in aerosol and cloud radiative  
99 effect. This work is the first attempt by the CERES team to evaluate clear-sky surface  
100 irradiances provided by its data products. One of the essential variables in computing  
101 clear-sky irradiances is aerosol optical depth. In this paper, we evaluate aerosol optical  
102 depth used for irradiance computations in the CERES project and analyze how the error  
103 propagates to clear-sky surface irradiances. Computations of surface irradiances provided  
104 by Edition 4.1 SYN1deg data products use aerosol optical depth derived by a chemical  
105 transport model [The Model for Atmospheric Transport and Chemistry (MATCH, Collins  
106 et al. 2001)] that assimilates MODIS-derived aerosol optical depth. The MATCH model  
107 is described in Section 1. In Section 2, we explain the aerosol transport model briefly. In  
108 Section 3, the assimilation of aerosol optical depth in the model is discussed. Sections 4  
109 and 5 compares aerosol optical depths used by the CERES team with, those from  
110 MERRA2 and the Aerosol Robotic Network (AERONET, Holben et al. 1998).

111

## 112       **2. Description of MATCH model**

113           The Model for Atmospheric Transport and Chemistry (MATCH) is a transport  
114 model of intermediate complexity driven by offline meteorological fields from the  
115 National Centers for Environmental Prediction (NCEP) reanalysis. It is run on a 194×96  
116 (1.9°×1.9°) spatial grid with a vertical resolution of 28 sigma-p levels. Temporally, the  
117 meteorological fields are linearly interpolated to 30-minute times at which time the



118 chemical processes are run. One exception is that the sulfur model is interpolated again to  
119 run at 2-min subscale time steps. MATCH is one of the many aerosol transport models  
120 that participated in the AeroCom model inter-comparison project (Textor et al., 2006;  
121 Kinne et al. 2006; Textor et al. 2007) and the AeroCom carbon inter-comparison project  
122 (Koch et al., 2009; Huneus et al., 2011).

123 Aerosol types included in MATCH are small dust, large dust, sulfate, sea salt,  
124 soot, soluble particles, and insoluble particles (**Table 1**). Model physics included in  
125 MATCH are parameterizations for convection and boundary layer processes, along with  
126 prognostic cloud and precipitation schemes for aqueous chemistry and the scavenging of  
127 soluble species. MATCH also includes the ability to resolve the transport of aerosols via  
128 convection, boundary layer transport, and scavenging and deposition of soluble gases and  
129 aerosols. MATCH can simulate most cloud processes currently in use in a GCM (eg.  
130 cloud fraction, cloud water and ice content, fraction of water converted to rain and snow,  
131 and evaporation of condensate and precipitate). It also includes vertical turbulent eddy  
132 processes. These processes are then used for convective transport, wet scavenging, wet  
133 deposition and dry deposition of the MATCH aerosols. These various parameterizations  
134 were developed, originally, for the NCAR Community Climate Model (CCM) and  
135 subsequently incorporated into the MATCH model. Descriptions of these  
136 parameterizations are given by Rasch et. al (1997, 2001), Collins et. al (2001) and  
137 additional papers described therein.

138 The MATCH aerosol suite includes a detailed mineral dust scheme in the Dust  
139 Entrainment and Deposition model, (Zender et al., 2003), and a diagnostic  
140 parameterization for sea-salt aerosol based on the 10m wind speed (Blanchard and



141 Woodcock, 1980). The sulfur cycle and the chemical reactions for sulfate aerosol creation  
142 rely on monthly climatological oxidant fields and emission inventories (**Table 1**) for  
143 sulfur oxides and oceanic dimethyl sulfide (photochemistry and nitrate aerosol are  
144 omitted). The reaction scheme is similar to that of the Model for Ozone and Related  
145 Chemical Tracers (MOZART), (Emmons et al., 2010). Carbon aerosols (both organic  
146 compounds and soot) evolve with simple mean lifetime e-foldings from surface fluxes  
147 specified through natural, biomass burning and fossil fuel burning emission inventories  
148 (also monthly climatologies given in **Table 1**).

Table 1. Aerosol Types & Climatological Sources

<i>Aerosol Type</i>	<i>Source</i>	<i>Description</i>
<i>Sea Salt</i>	Blanchard and Woodcock, 1980	Wind Driven
<i>Dust</i>	Ginoux et al. (2001); Zender et al. (2003)	NCEP soil moisture, wind driven
<i>Sulfate (natural &amp; anthropogenic)</i>	Benkovitz et al. (1996); Barth et al. (2000)	monthly climatological
<i>Carbon (organic &amp; Soot)</i>	Liousse et al. (1996)	monthly climatological
<i>Volcanic</i>	Episodic inclusion of Sulfur dioxide	Processed by model

149

150 The optical properties of the various aerosol types (e.g. mass extinction  
151 coefficient, single scatter albedo), which are key parameters for aerosol assimilation, are  
152 drawn from the standard Optical Properties of Clouds and Aerosols (OPAC, Hess et al.  
153 1998) database. Scattering properties from MATCH are not used directly in the radiative  
154 transfer calculations in the SYN1deg. Instead, aerosol types from MATCH are mapped to  
155 a similar set of scattering properties embedded in the Langley Fu & Liou radiative  
156 transfer code (Fu and Liou, 1993; Fu et. al 1998; Rose et. al 2013). These include OPAC



157 as in MATCH for all but the small and large dust particles. Dust scattering and absorption  
158 properties in the Langley Fu & Liou code are from Sinyuk et al. (2003).

159

## 160 **2.1 MATCH Assimilation of MODIS Aerosol Optical Depths**

161 One major advantage of the MATCH model is its ability to reliably assimilate  
162 satellite-based retrievals of aerosol optical depth (AOD) to constrain the climatologically  
163 forced aerosols generated within the chemical transport portion of the code. Edition 4  
164 MATCH algorithms ingest MODIS Collection 6.1 AOD (Remer et al., 2005), beginning  
165 in March 2000 from the Terra satellite and June 2002 from both Terra and Aqua  
166 satellites. The MATCH assimilates MODIS AOD at the green wavelength of 550 nm.  
167 MATCH combines AOD derived by the Dark Target (Levy et al. 2013) and Deep Blue  
168 algorithms (Hsu et al., 2006). A global daily mean AOD in a 1.9°x1.9° grid is derived  
169 from Terra and Aqua observations by simply averaging available Terra and Aqua dark  
170 target and deep blue derived AODs in a grid box. Unlike dark target and deep blue  
171 merged product (MOD08), we do not use a quality assurance confidence (QAC) score to  
172 screen AOD.

173 Because Terra and Aqua overpass time is 10:30 AM and 1:30 PM local time,  
174 AOD at local solar noon is assimilated by taking a 15° longitude width of retrieved AOD  
175 from the daily mean map. Examples of the magnitude of AOD adjustments by the  
176 assimilation are shown in **Fig. 1**. **Figure 1a** shows hourly AOD field differences, 4 UT  
177 minus 3 UT on February 1<sup>st</sup>, 2020. Similarly, **Figure 1b** shows 10 UT minus 9 UT of the  
178 same day. The 15° vertical band is clearly visible where red (blue) colors indicate total  
179 column aerosol is increased (decreased) by the MODIS AOD assimilation. Following the





180 AOD adjustment, aerosol masses in the atmospheric column through the troposphere are  
181 scaled to closely match the AOD derived from MODIS. Neither the vertical profile nor  
182 the relative abundance of the aerosol species is adjusted. Once aerosol mass is adjusted at  
183 the local noon for the regions where MODIS AOD is available, the adjusted aerosol mass  
184 is carried on to the next time step. Besides the MODIS adjustments, wind driven sea-salt  
185 creation and deposition are found along frontal boundaries in the North Atlantic and  
186 Southern Oceans. The maps also indicate hourly increases and decreases in high aerosol  
187 loading areas such as those found around China and SE Asia.

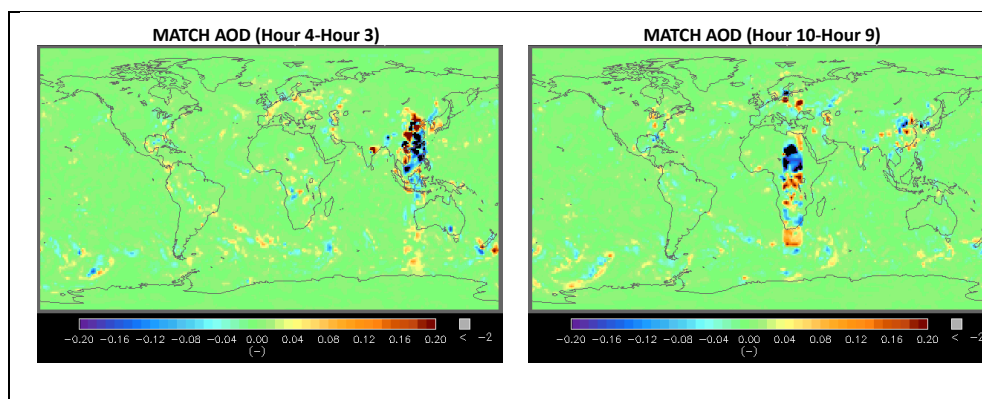


Figure 1. Difference of MATCH AOD due to the assimilation of MODIS AOD. The left plot is 4 UT minus 3 UT and right plot is 10 UT minus 9 UT on February 1, 2020. AOD is adjusted at the local solar noon within the 15° longitudinal band by the MODIS AOD assimilation. Wind-blown dust and sea salts differences are also apparent outside the 15° longitudinal band.

188

189 Episodic events such as intense fires or volcanic eruptions are not specifically  
190 included in the MATCH aerosol package. Such events are captured by the assimilation of  
191 MODIS AOD and total column aerosol loading is adjusted upward. The adjustment is  
192 applied to AOD only. The aerosol type (and so scattering properties) is not adjusted to  
193 reflect the reality of the scattering or absorbing aerosol during such an event.

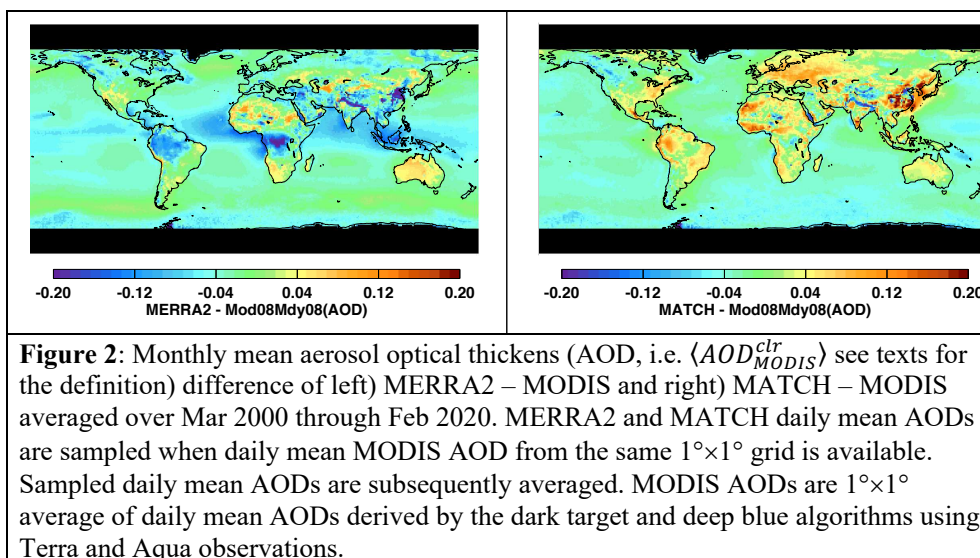
194



195

## 196 **2.2 MATCH and MERRA2 comparison**

197 In this section, we compare AODs between MATCH and MERRA2 (Randles et  
198 al., 2017) in which MODIS clear-sky radiances are assimilated. MERRA2 also  
199 assimilates surface observed AOD by AEROENT and ship born AOD observations. We  
200 compare AODs in two different ways. First, MATCH and MERRA2 AODs are compared  
201 with MODIS AODs. The first comparison tests the consistency of daily means when  
202 MODIS aerosol optical depth is available (i.e. clear somewhere in the grid box at Terra  
203 and Aqua overpass time). Second, MATCH and MERRA2 AODs are compared under  
204 all-sky conditions, which is only possible with modeled AODs.



205

206 **Figure 2** shows differences of monthly mean AOD between MERRA2 and  
207 MODIS on the left and MATCH and MODIS on the right. To compute the monthly mean  
208 AOD differences, both MERRA2 and MATCH daily mean AODs are sampled when  
209 daily mean MODIS AOD from the same  $1^\circ \times 1^\circ$  grid is available (hereinafter  $AOD_{MODIS}^{clr}$ ).



210 Sampled daily mean AODs ( $AOD_{MODIS}^{clr}$ ) are subsequently averaged (hereinafter  
211  $\langle AOD_{MODIS}^{clr} \rangle$ , where the bracket indicates a simple arithmetic monthly mean). Although  
212 both products assimilate MODIS observations, each shows fairly significant differences  
213 from MODIS values. Differences arise because MODIS daily mean AOD is clear-sky  
214 AOD at Terra and Aqua overpass time only while MERRA2 and MATCH daily mean  
215 AOD includes AOD from other times of the day. When the non-overpass time is also  
216 clear, MATCH  $AOD_{MODIS}^{clr}$  should be close to MODIS  $AOD_{MODIS}^{clr}$ . However, when clouds  
217 are present in MATCH during non-overpass times, modeled AOD are used, hence the  
218 daily mean AOD can deviate from MODIS  $AOD_{MODIS}^{clr}$ . In addition, AOD differences for  
219 MERRA2 at Terra and Aqua overpass times might be larger than MATCH even for clear-  
220 sky conditions as MERRA2 assimilates observed AOD data other than MODIS AOD.

221 While MATCH shows large positive differences over land, especially China and  
222 south east Asia, Australia, Amazon, and north Africa, MERRA2 shows significantly  
223 negative differences over major rain-forest regions of south America, Africa, and the  
224 tropical western Pacific. Both  $\langle AOD_{MODIS}^{clr} \rangle$  are closer to MODIS AOD over ocean  
225 compared to  $\langle AOD_{MODIS}^{clr} \rangle$  over land except MERRA2 shows a negative difference across  
226 the Indian ocean and off the west coast of Africa in the Atlantic Ocean. When MODIS  
227  $AOD_{MODIS}^{clr}$  is available in the grid box, MATCH weighs MODIS AOD heavily in  
228 assimilating MODIS AOD at local solar noon so that MATCH AOD is nearly identical to  
229 MODIS AOD at the local noon under clear-sky regions. As a consequence, the difference  
230 of global monthly mean MATCH and MODIS  $AOD_{MODIS}^{clr}$  is smaller than the difference  
231 of MERRA2 and MODIS  $AOD_{MODIS}^{clr}$ .



232 **Figure 3** shows the difference of  $AOD_{MODIS}^{clr}$  more clearly. In **Fig. 3**  $AOD_{MODIS}^{clr}$  are  
 233 compared directly in a log-density plot where each point represents a comparison for the  
 234 daily average of a given grid box; MERRA2 versus MODIS on the left and MATCH  
 235 versus MODIS on the right. **Figure 3** indicates that MATCH  $AOD_{MODIS}^{clr}$  has a smaller  
 236 bias with respect to the MODIS AOD than the MERRA2 AOD but has approximately the  
 237 same RMS compared to the MERRA2  $AOD_{MODIS}^{clr}$ .

238  
 239

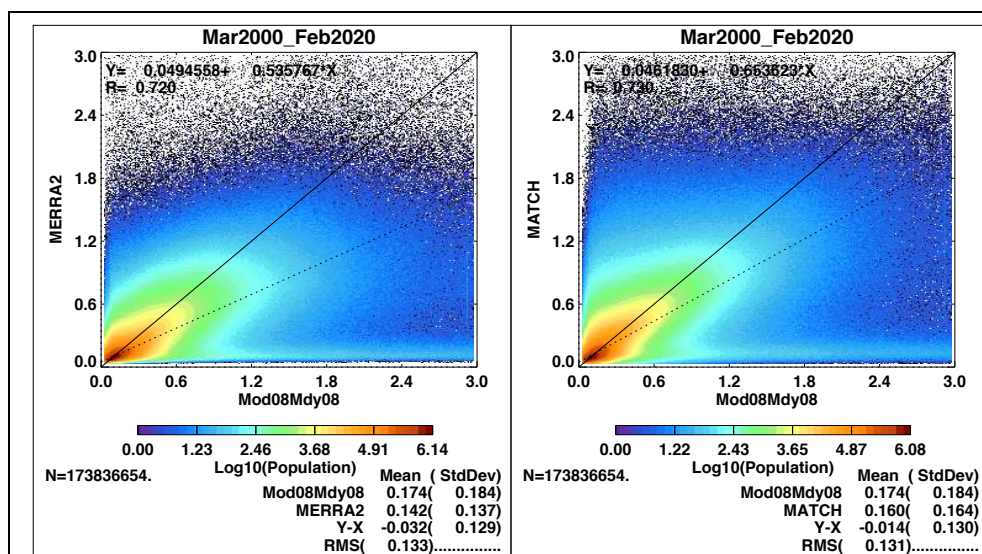


**Figure 3:** Scatter plot of daily  $1^\circ \times 1^\circ$  mean aerosol optical depth (AOD) from a) MERRA2 and b) MATCH versus AOD derived from MODIS on Terra and Aqua for Mar 2000 through Feb 2020. MODIS AODs are  $1^\circ \times 1^\circ$  daily average of AODs derived by the dark target and deep blue algorithms. Only days and grid boxes that have MODIS AOD (i.e.  $AOD_{MODIS}^{clr}$  defined in the texts) are used.

240  
 241  
 242

**Figure 4** shows  $1^\circ \times 1^\circ$  monthly mean maps of MATCH AOD on the left and its  
 243 difference from MERRA-2 on the right for all sky (top maps) and clear sky (bottom  
 244 maps) conditions for March 2000 through February 2020. The clear-sky monthly mean  
 245 aerosol optical depth is derived by averaging daily mean aerosol optical depth weighted



246 by clear fraction (hereinafter  $\overline{AOD_{MODIS}^{clr}}$ , overbar indicates monthly mean), where the  
247 clear fraction is derived from MODIS on Terra and Aqua (Minnis et al. 2020). MATCH  
248 all-sky AOD (hereinafter  $\overline{AOD^{all}}$ ) is larger than MERRA2  $\overline{AOD^{all}}$ , particularly over the  
249 rain forest regions of the globe as well as India and China. Although the difference is  
250 smaller, the difference of  $\overline{AOD_{MODIS}^{clr}}$  shows a similar spatial pattern (**Fig. 4** bottom right)  
251 to the all-sky difference. This is consistent with **Fig. 2**, showing that MERRA2 tended to  
252 underestimate  $AOD_{MODIS}^{clr}$  with respect to MODIS  $AOD_{MODIS}^{clr}$ . A larger difference over  
253 convective regions (e.g. Amazon, central Africa, and south east Asia) is caused by how  
254 dark target and deep blue AOD are merged. As mentioned earlier, we do not use QAC to  
255 screen AOD. Convective clouds introduce a larger uncertainty to AOD because of a 3D  
256 radiation effect or poor fit to observations with retrieved AOD (personal communication  
257 with R. Levy 2020). For these situations, AODs associated with QA confidence scores  
258 less than 2 are screened out in the MOD08 dark target and deep blue merged product  
259 (Levy et al. 2013).  
260

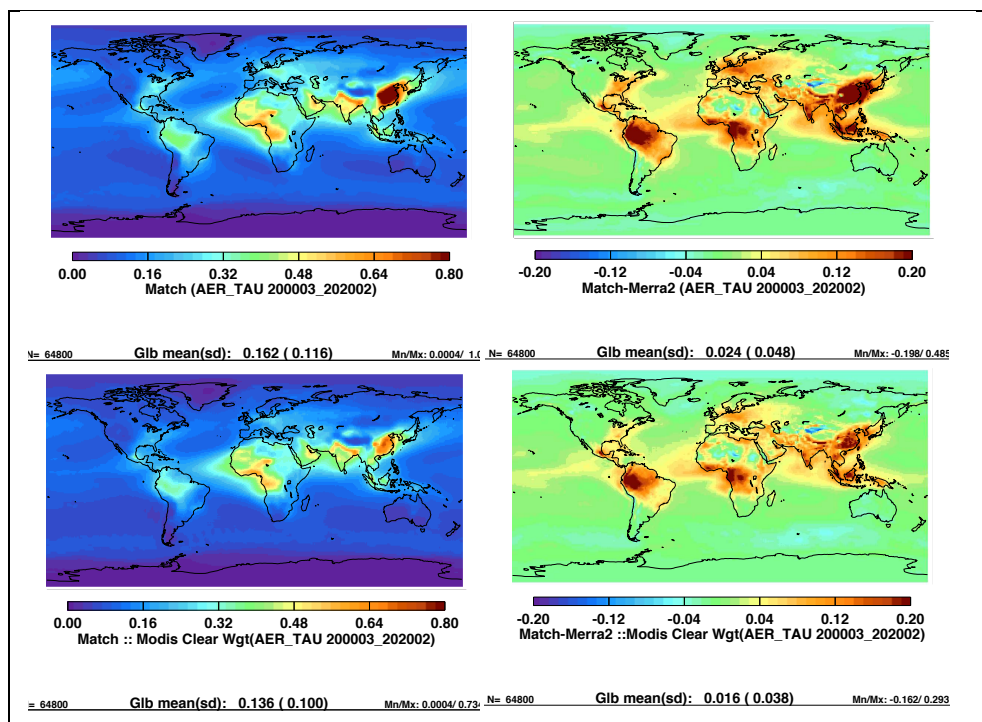


**Figure 4.** Left) Monthly mean aerosol optical depth (AOD) from MATCH and right) the difference between MATCH and MERRA2 (MATCH – MERRA2) for January 2020. Top maps are for all-sky (i.e.  $AOD_{MODIS}^{all}$ , bottom maps are for clear-sky (i.e.  $AOD_{MODIS}^{clr}$ ). Clear-sky monthly mean aerosol optical depth is derived by averaging daily mean aerosol optical depth weighted by daily  $1^\circ \times 1^\circ$  gridded mean clear fraction where the clear fraction is derived from MODIS on Terra and Aqua.

261

### 262 2.3 Comparison with AERONET

263 Above results indicate that both MATCH and MERRA2  $\overline{AOD_{MODIS}^{clr}}$  are

264 generally, respectively, larger and smaller than MODIS  $\overline{AOD_{MODIS}^{clr}}$ . Larger difference

265 between MATCH and MERRA2  $\overline{AOD^{all}}$  over convective regions originated from

266 merged AOD product used for the assimilation. Of primary importance to radiative

267 transfer calculations within the SYN1deg product is the ability of the MATCH model to

268 accurately represent total column aerosol optical depth. To test the overall accuracy, we

269 use observations from the AERosol RObotic NETwork (AERONET). AERONET is a



270 global federation of ground-based remotes sensing sites developed by NASA and now  
271 supported by a number of institutions around the world (Holben et al. 1998). Each site  
272 maintains a CIMEL sun-photometer that scans the daytime sky every 20 minutes.  
273 Collected data are processed according to standards of calibration and processing  
274 maintained by the AERONET project. Here we utilize Level 2.0, data that have been  
275 screened for clouds and quality assured (Smirnov et al. 2000).

276 **Figure 5** shows an hourly time series of AOD from MATCH, MERRA2 and  
277 AERONET for January 2010 at the Beijing China AERONET site. The top plot shows  
278 cloud fraction time series derived from MODIS and GEOs from the SYN1deg Ed4.1  
279 product (Rutan et al. 2015), and the bottom plot shows AOD time series. Generally, both  
280 models produce a large variability of AOD at this site fairly well over the course of the  
281 month. While both MERRA2 and MATCH AODs increase near times when cloud  
282 fraction approaches 100%, the increase of MATCH AOD, which correlates with the  
283 increase of AERONET AOD relatively well, is larger than the increase of MERRA2  
284 AOD. Although the temporal correlation coefficient of the MATCH and AERONET  
285 AODs is smaller at this site during summer months than during winter months (not  
286 shown), a good temporal correlation between MATCH and AERONET AODs is  
287 consistent across most locations and times we considered. To show this statistically, in  
288 the following, we extend this analysis to a number of AERONET sites grouped  
289 geographically based on general aerosol type.  
290

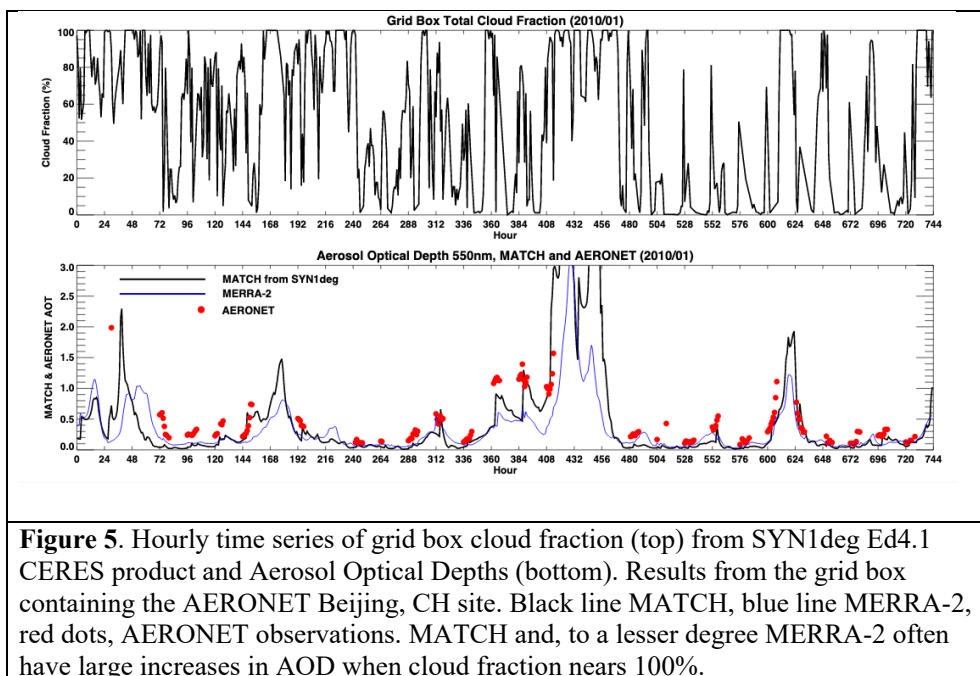


**Figure 5.** Hourly time series of grid box cloud fraction (top) from SYN1deg Ed4.1 CERES product and Aerosol Optical Depths (bottom). Results from the grid box containing the AERONET Beijing, CH site. Black line MATCH, blue line MERRA-2, red dots, AERONET observations. MATCH and, to a lesser degree MERRA-2 often have large increases in AOD when cloud fraction nears 100%.

291  
292

293           Aerosol optical depths from AERONET are nominally provided at 8 spectral  
294 channels, every 20 minutes given favorable conditions. We use two channels to derive  
295 observed AOD at 550 nm to compare to the AOD provided by the MATCH model.  
296 Because the SYN1deg radiative transfer calculation is done hourly, we average any  
297 observations within a given hour period centered at the 30<sup>th</sup> minute for each site  
298 collocated within a SYN1deg grid box. AERONET sites chosen are shown in **Fig. 6** with  
299 a complete listing of all sites in Appendix 1. Though we examine 45 sites over 20+ years,  
300 we aggregate the statistics within continental regions which naturally isolates them by  
301 general climatic conditions. Tables 2 and 3 show comparisons for each site grouping,  
302 respectively, for clear sky (less than 1% cloud identified by MODIS and geostationary  
303 satellites in the SYN1deg grid box) conditions and for all sky (any cloud condition within





304 the SYN1deg grid box) conditions. Using clear-sky scenes identified by MODIS only  
305 gives the same statistical results with fewer number of samples. Statistics shown in  
306 Tables 2 and 3 are the average observed value, mean bias (MATCH – Observation), root  
307 mean square (RMS) difference and the correlation coefficient (R) over the time period  
308 from March 2000 through February 2020. The actual time period varies depending on the  
309 site due to AERONET data availability. The RMS difference and correlation coefficient  
310 are computed by each site with hourly mean values where observations are available  
311 from March 2000 through February 2020. For comparison purposes we show the same  
312 statistics derived from observations compared to MERRA2 AODs using the identical  
313 hours. We note, however, that MERRA2 assimilates AERONET while MATCH AODs  
314 are independent from AERONET AODs.

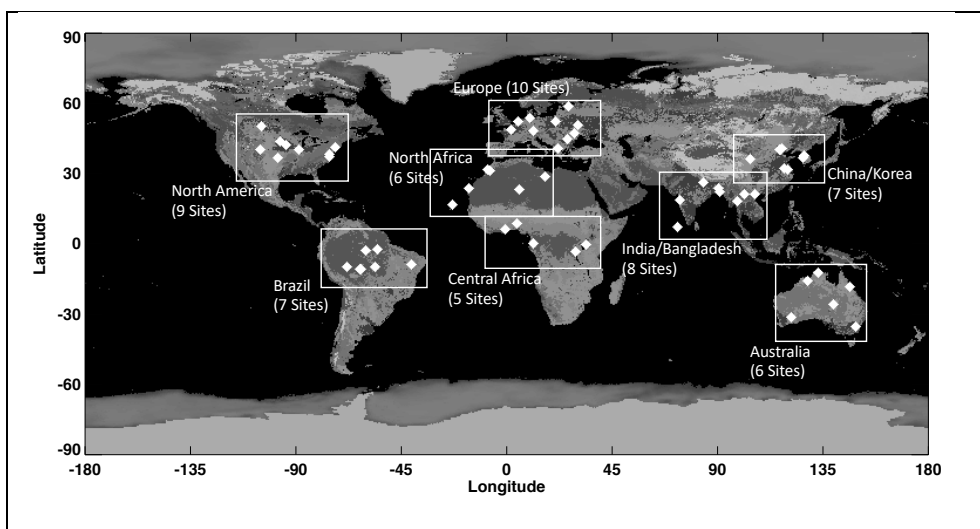


**Figure 6.** Location of AERONET sites and how they grouped for calculations of mean/bias/RMS with respect to MATCH and MERRA-2 optical depths found in tables 2 and 3.

315

316 MATCH AOD for the Brazil group is biased high by 0.03, and China south east

317 Asia has no bias compared with AREONET AODs. These two regions have relatively



318 large bias of  $\langle AOD_{MODIS}^{clr} \rangle$  from MATCH compared with MODIS AODs (**Fig. 2** right). In  
319 contrast, negative bias of MERRA2 AODs compared with AERONET AODs for Brazil,  
320 central Africa, and China/South East Asia groups are consistent with negative bias of  
321 MERRA2  $\langle AOD_{MODIS}^{clr} \rangle$  compared with MODIS AODs (**Fig. 2** left). For the China/south  
322 east Asia group, the RMS difference between MATCH AODs and AERONET AODs is  
323 0.18 and correlation coefficient is 0.7. These are worse than the counterpart values of  
324 MERRA2 versus AERONET AODs because summertime agreement between MATCH  
325 and AERONET AODs is worse if a similar plot as **Fig. 5** is plotted for summertime when  
326 hygroscopic aerosols are dominant under high relative humidity conditions.

327         The sign of the MATCH AODs compared to AERONET AODs for all-sky  
328 conditions is generally consistent with the sign of clear-sky counterparts. The RMS  
329 difference under all-sky conditions is generally larger than the clear-sky RMS difference  
330 while the correlation coefficient is nearly the same. The biases for MERRA2  
331 comparisons are generally comparable to MATCH though RMS for MERRA2 tend to be  
332 slightly smaller and correlations tend to be higher due in part to the assimilation of  
333 AERONET into the MERRA2 model.

334

335

336

337

338

339

340



Table 2. Hourly AERONET station statistics for MATCH and MERRA-2.  
 Continental Groups, Clear Sky conditions<sup>1</sup>

Site	MATCH						MERRA-2		
	Predominant Aerosol Type	Number	Observed Average	Bias	RMS	R <sup>2</sup>	Bias	RMS	R <sup>2</sup>
<i>Australia (5 Sites)</i>	Dust Smoke	20925	0.06	0.01	0.06	0.4	0.03	0.05	0.7
<i>Brazil (7 Sites)</i>	Smoke Polluted	6554	0.14	0.02	0.10	0.8	-0.02	0.08	0.9
<i>Central Africa (5 Sites)</i>	Smoke	2139	0.70	-0.10	0.24	0.9	-0.10	0.24	0.9
<i>North Africa (5 Sites)</i>	Dust	10047	0.17	0.07	0.15	0.7	0.02	0.10	0.8
<i>China SE Asia (8 Sites)</i>	Polluted	2827	0.26	-0.00	0.18	0.7	-0.03	0.15	0.8
<i>India/Bangladesh (6 Sites)</i>	Smoke Polluted	3010	0.51	-0.09	0.28	0.6	-0.10	0.24	0.8
<i>North America (9 Sites)</i>	Continental Polluted	21429	0.10	-0.00	0.07	0.7	0.00	0.06	0.8
<i>Europe (10 Sites)</i>	Continental Polluted	10211	0.13	0.01	0.07	0.7	-0.02	0.05	0.8

<sup>1</sup>The time period used is from Mar 2000 through Apr 2020. Actual period varies by site depending on AERONET data availability. Clear Sky is identified by MODIS and geostationary satellites and the cloud fraction is less than 1% over a SYN1deg grid box.

341  
 342  
 343  
 344  
 345  
 346  
 347  
 348  
 349  
 350  
 351  
 352  
 353  
 354

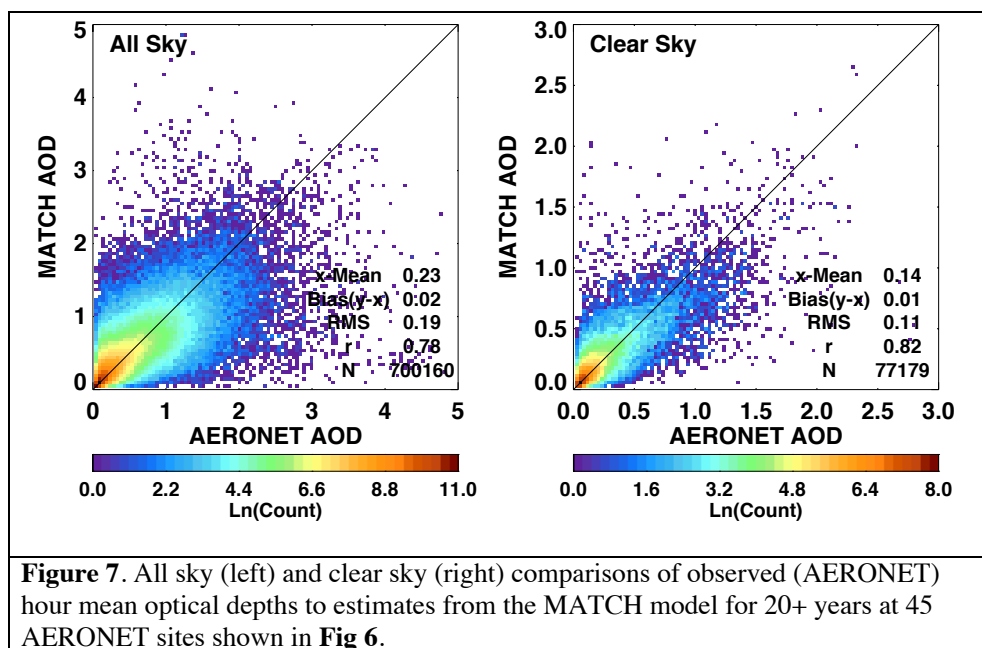


Table 3. Hourly AERONET station statistics for MATCH and MERRA-2. Continental Groups, All Sky Conditions<sup>1</sup>

Site	Predominant Aerosol Type	Number	Observed Average	MATCH			MERRA-2		
				Bias	RMS	R <sup>2</sup>	Bias	RMS	R <sup>2</sup>
Australia (5 Sites)	Dust Smoke	110523	0.09	0.00	0.09	0.5	0.02	0.07	0.8
Brazil (7 Sites)	Smoke Polluted	72656	0.25	0.03	0.23	0.8	-0.04	0.18	0.9
Central Africa (5 Sites)	Smoke	41193	0.55	-0.07	0.26	0.8	-0.10	0.26	0.9
North Africa (5 Sites)	Dust	43205	0.23	0.08	0.20	0.7	0.01	0.14	0.8
China SE Asia (8 Sites)	Polluted	52287	0.45	0.01	0.31	0.7	-0.08	0.27	0.8
India/Bangladesh (6 Sites)	Smoke Polluted	44534	0.61	-0.06	0.32	0.6	-0.10	0.32	0.7
North America (9 Sites)	Continental Polluted	160356	0.13	0.02	0.13	0.6	0.00	0.09	0.7
Europe (10 Sites)	Continental Polluted	175010	0.18	0.04	0.14	0.6	-0.02	0.08	0.8

<sup>1</sup> The time period used for the statistics is from March 2000 through April 2020. The actual period varies by site depending on AERONET data availability.  
<sup>2</sup> Correlation coefficient.

355  
 356





357

358 Results for all points across all sites and times are shown in **Fig. 7**. The color  
359 density plots are in log scale and indicate the vast majority of observations have an AOD  
360 of less than one for both clear and all sky conditions observed within the SYN1deg grid  
361 box. Biases are less than 10% of the mean value but RMS is large relative to the mean  
362 observed value. Overall correlation is approximately 0.8. The ‘clear sky’ hours (where  
363 SYN1deg estimated less than 1% cloud in the grid box based on MODIS and GEO  
364 observations) is a little more than 10% of the overall points. When MATCH AOD is  
365 compared to MERRA2 AOD (not shown) MATCH is biased approximately 10% higher.

366

### 367 **3. Discussion of AOD Differences**

368 In this section, we investigate the reason for the AOD differences shown in the  
369 previous section. In addition, we estimate the effect of the AOD differences to surface  
370 irradiances when MATCH AODs are used for surface irradiance computations.

371 Generally, cloud contamination in MODIS AODs is caused by unresolved sub-  
372 pixel scale clouds (Kaufman et al. 2005; Martins et al. 2002). The difference shown over  
373 convective regions, therefore, seems to be caused by the uncertainty due to 3D radiative  
374 effects that impact retrieved AODs by unknown amounts (Wen et al. 2007), by errors in  
375 estimating the fraction of hygroscopic aerosols or by the errors in estimating water uptake  
376 by hygroscopic aerosols (Su et al 2008). Larger AODs are screened out in the MOD08  
377 data product while the CERES team uses all retrieved AODs regardless of the QAC  
378 score. The comparison with AERONET AODs is not decisive to determine how to screen  
379 MODIS AODs because MATCH AODs are positively biased and MERRA2 AODs are  
380 negatively biased for the Brazil group. The result underscores the difficulty of deriving



381 accurate AODs, which appear to involve requirements in addition to identification of  
382 clear-sky scenes. Levy et al. (2013) list reasons lowering the QAC score as 1) pixels are  
383 thrown out due to cloud masking, 2) retrieval solution does not fit the observation well,  
384 and 3) the solution is not physically plausible given the observed situation. Therefore,  
385 even though the difficulty of identifying clear-sky scenes is driven by cloud  
386 contamination by trade cumulus (Loeb et al. 2018), the difficulty of deriving AODs exists  
387 over convective regions (Varnai et al., 2017).

388         Larger positive biases of MATCH AODs compared with AERONET AODs exist  
389 over Africa (Tables 2 and 3). For North Africa, the bias is known to be caused excessive  
390 dust generated by the MATCH algorithm. Even though modeled aerosols are not often  
391 used over north Africa owing to the abundance of clear-sky conditions, the dust problem  
392 leads to a larger positive AOD bias. In addition, MATCH uses fixed aerosol sources in  
393 time. Therefore, it tends to miss large aerosol events, such as forest fires, until clear-sky  
394 conditions occur, allowing observations of the event by MODIS. This leads to a larger  
395 RMS difference and lower correlation coefficient with AERONET AODs compared with  
396 those from MERRA2 versus AERONET.

397         Because MODIS AOD are not generally available under overcast conditions, the  
398 reliance on modeled AOD increases as the cloud fraction over a  $1^\circ \times 1^\circ$  grid increases.

399 **Figure 5**, which shows that AERONET AOD increases with cloud fraction derived from  
400 satellites, indicates that as the cloud fraction over a  $1^\circ \times 1^\circ$  grid increases, AOD over the  
401 clear-sky portion of the grid increases. In addition, **Fig. 5** suggests that modeled AODs  
402 under near overcast conditions are significantly larger than clear-sky AODs that are  
403 constrained by MODIS observations. Because we are not able to evaluate AODs under



404 overcast conditions, here we only assess AOD changes with cloud fraction using ground-  
405 based observations. **Figure 8** shows the distribution of AERONET AODs for clear-sky  
406 and all-sky conditions, as well as precipitable water derived from a microwave  
407 radiometer separated by these two conditions. Clear-sky is identified by the Long-  
408 Ackerman algorithm (Long et al. 2006) that uses surface direct and diffuse irradiances.  
409 **Figure 8** shows that AOD and precipitable water under all-sky conditions are  
410 significantly larger than those under clear-sky conditions. When we use cloud fraction  
411 derived from satellite and plot AOD and precipitable water as a function of the cloud  
412 fraction using the same grid box where the ground site is located, AOD and precipitable  
413 water increase with the cloud fraction (**Fig. 9**). Therefore, increasing AOD with cloud  
414 fraction shown in **Fig. 5** is qualitatively explained by increasing AOD of hygroscopic  
415 aerosols with relative humidity. However, **Fig. 9** indicates that either the growth of  
416 MATCH AOD seems to be too strong or modeled MATCH AOD under all-sky  
417 conditions is too large.  
418

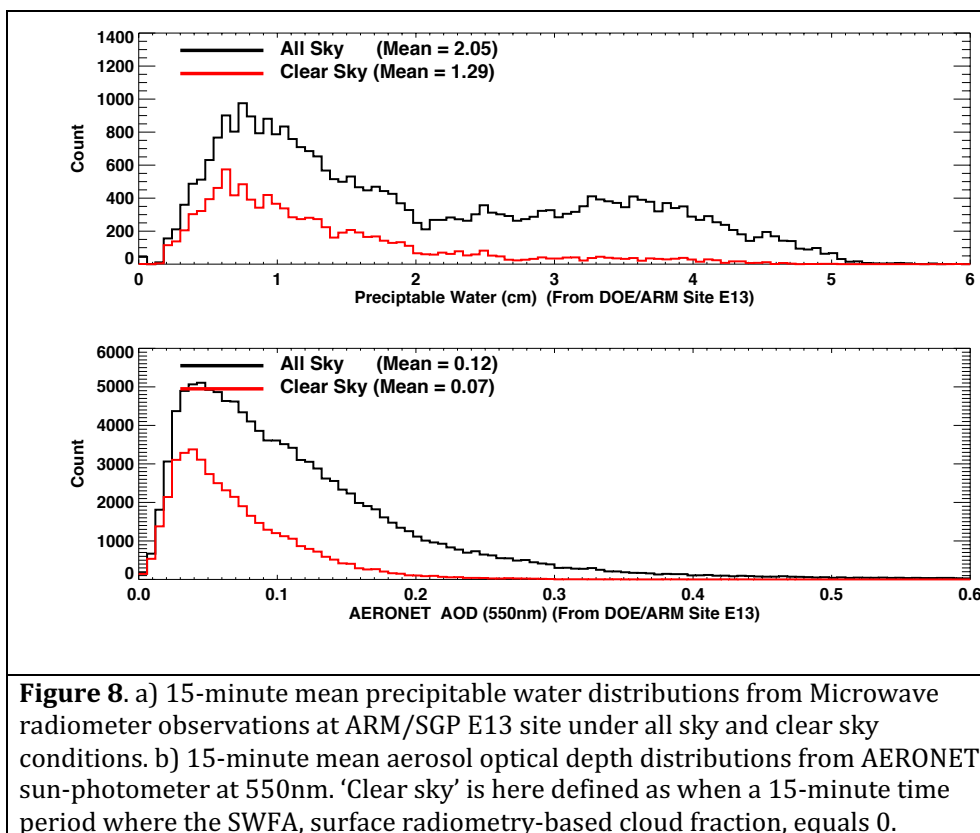


**Figure 8.** a) 15-minute mean precipitable water distributions from Microwave radiometer observations at ARM/SGP E13 site under all sky and clear sky conditions. b) 15-minute mean aerosol optical depth distributions from AERONET sun-photometer at 550nm. ‘Clear sky’ is here defined as when a 15-minute time period where the SWFA, surface radiometry-based cloud fraction, equals 0.

419

420

421



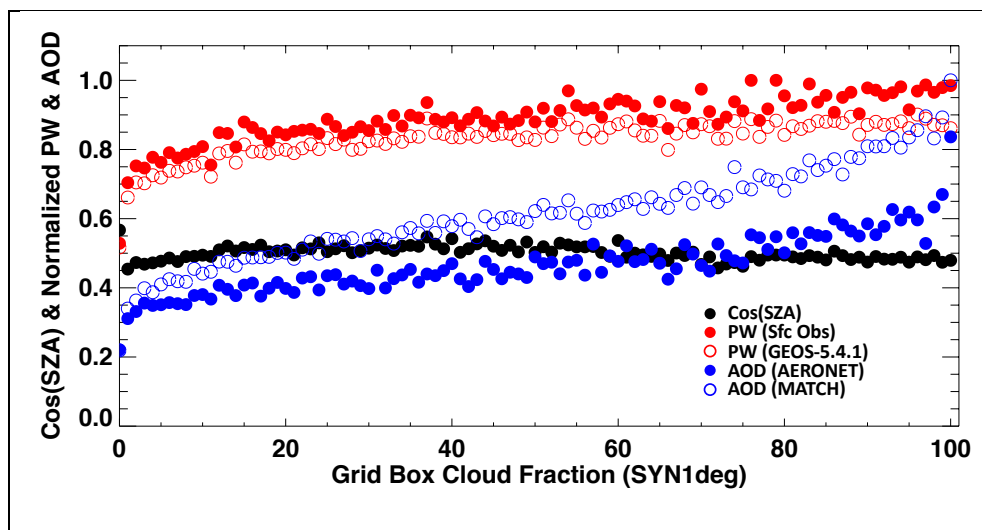


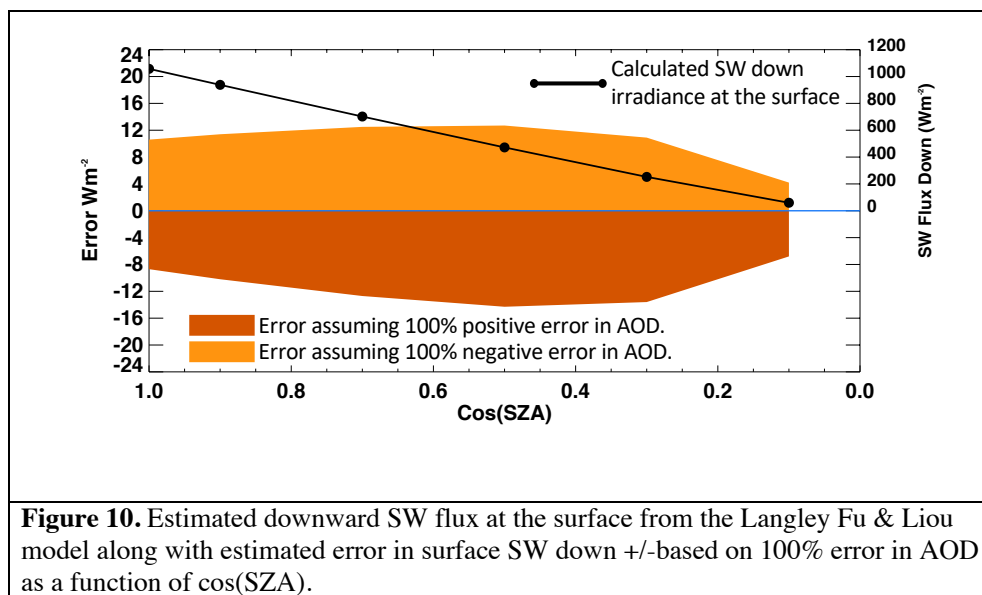
**Figure 9.** Aerosol optical depth (AOD) and precipitable water (PW) as a function of cloud fraction over the  $1^\circ \times 1^\circ$  grid box where the ARM/SGP E13 and SURFRAD Bondville IL sites are located. Closed and open blue circles are, respectively, AOD derived from AERONET and MATCH AOD. Closed and open red circles are, respectively, PW derived from microwave radiometer and CIMEL sun photometer and GEOS-5.4.1 PW. Cloud fractions are derived from MODIS and geostationary satellites. Black dots are mean cosine solar zenith angle of the time of AOD and PW observations. AOD and PW are normalized to their maximum value for display.

422

423

424

425



426

427

### 428 **3.1 Effect of AOD differences on surface irradiances**

429 **Figure 10** shows a summary of a series of radiative transfer calculations using the

430 “On-Line Langley Fu & Liou radiative transfer code:

431 [https:// cloudsgate2.larc.nasa.gov/cgi-bin/fuliou/runfl.cgi](https://cloudsgate2.larc.nasa.gov/cgi-bin/fuliou/runfl.cgi)

432 with an open shrub spectral albedo (broadband albedo of 0.14 at  $\mu_0=1.0$ ), “continental”

433 aerosol, and no clouds. Values on the solid black line are the calculated surface

434 downward irradiances with an AOD of 0.09 at six different solar zenith angles.

435 Calculations were then done for AOD’s of 0.0 and 0.18, at the same solar zenith angles,

436 representing 100% error bounds of the mean AODs derived from AERONET (as seen in

437 Tables 2 and 3 for the Australia sites where the RMS is approximately equal to the

438 observed average of AOD). The orange and red shaded areas indicate potential bias of

439 the downward shortwave irradiance at a given solar zenith angle. Irradiance values scale



440 nearly linearly between these limits. **Figure 8** shows the error remains nearly constant  
441 until a  $\mu_0=0.5$  where it begins to decrease as insolation decreases. However, due to longer  
442 path lengths at large solar zenith angles, the percentage error actually increases.

443

#### 444 **4. Clear Sky Comparisons of SYN1deg and Surface Observed Irradiances**

445 We complete our analysis of the impact of the MATCH aerosols on computed  
446 surface irradiances by comparing calculated hourly mean surface downward shortwave  
447 irradiance from the Ed4.1 SYN1deg-Hour product to observations of downward  
448 shortwave irradiances. In a  $1^\circ \times 1^\circ$  grid box with an approximate size of 111 km  $\times$  111 km,  
449 100% clear sky sampled over one hour as determined by MODIS or geostationary  
450 satellites is relatively rare. None the less, by grouping sites based on general surface  
451 conditions and analyzing 20 years of data sufficient samples are found. **Figure 11** shows  
452 the sites as grouped by color including 15 land sites labeled “Mid-Latitude” (Green  
453 triangles), 6 sites labeled “Desert” (Red), 6 sites labeled “Polar” (White) and 46 buoys  
454 (Blue). Surface observed SW irradiance from the land sites comes from the Baseline  
455 Surface Radiation Network (Ohmura et al. 1998; Dreimel et al. 2018) and buoy data are  
456 made available

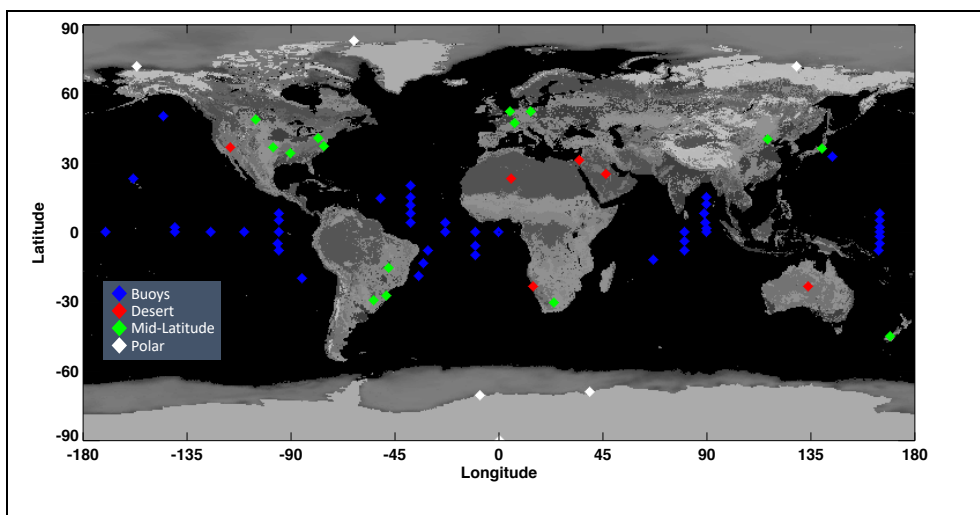


**Figure 11.** Location of surface observations of downwelling shortwave irradiance used to compare the SYN1deg Ed4.1 calculations to observations for all available hours (from Mar 2000 through Dec 2019) where the SYN1deg cloud analysis determines the hour to be 100% clear sky.

457

458 from the Pacific Marine Environmental Lab (PMEL) (McPhaden et al. 2002, 2009) and  
459 the Woods Hole Oceanographic Institute (WHOI) (Colbo and Weller, 2009). A complete  
460 listing is given in Appendix A.

461 **Figure 12** shows hourly comparisons of computed clear-sky downward  
462 shortwave irradiance compared to observations for the four groups of sites shown in **Fig.**  
463 **11**. In general, the calculated irradiance is larger than observed downward shortwave  
464 irradiance. There we find that in every grouping, SYN1deg calculations tend to be too  
465 transmissive, overestimating the surface downwelling SW irradiance by between  $4 \text{ Wm}^{-2}$   
466 (polar sites) and  $16 \text{ Wm}^{-2}$  (ocean buoys) with mid-latitude and desert sites each  
467 overestimating DSF by  $\sim 10 \text{ Wm}^{-2}$ . It's notable that the smallest overestimation is in polar  
468 regions where column AOD would be the smallest. This points to the possibility that  
469 MATCH is weighted too far towards scattering aerosols and too few absorbing aerosols.

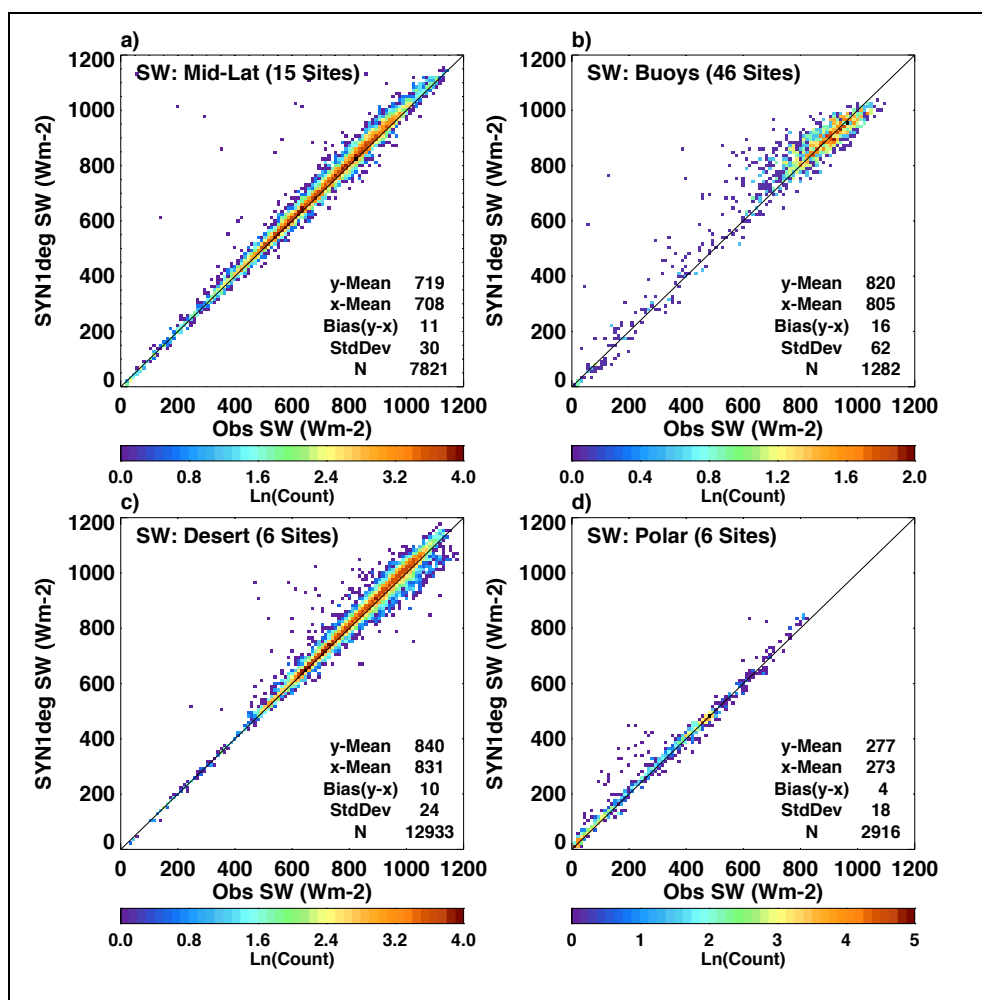


**Figure 12** Comparisons of SW downward irradiance at the surface from the SYN1deg Ed4.1 calculations (y-axis for all plots) and BSRN and buoy surface sites (x-axis all plots). Data are from Mar 2000 through Feb 2020 and only include hours when a 1x1 grid box is 100% clear-sky according to SYN1deg cloud fraction.

470

471

Clear-sky scenes used for **Fig. 12** are those identified by MODIS and

472

geostationary satellites over the  $1^\circ \times 1^\circ$  grid where the ground site located. That is, when

473

the satellites did not detect clouds over the one-hour period within the grid box, we

474

compared the computed and observed hourly mean downward shortwave irradiances.

475

Clouds might have been present within the field-of-view of the ground-based



476 pyranometer but not within the field of view of sun-photometer. This would increase the  
477 observed downward shortwave irradiance, hence the modeled irradiance would be  
478 smaller. To verify, we used the ground-based cloud screening algorithm developed by  
479 Long and Ackerman (Long et al. 2006) to further screen clouds. For the land groupings,  
480 plots showing the difference between calculation minus observation as a function of  
481 observation, utilizing both the satellite and surface based observed cloud fraction to 0.0,  
482 are shown in **Fig. 13**. As shown in the plot, mean bias did not change significantly.  
483 However, the RMS in both the Mid-Latitude and Desert sites was reduced by half due to  
484 the more stringent cloud screening (**Fig. 13**).

485

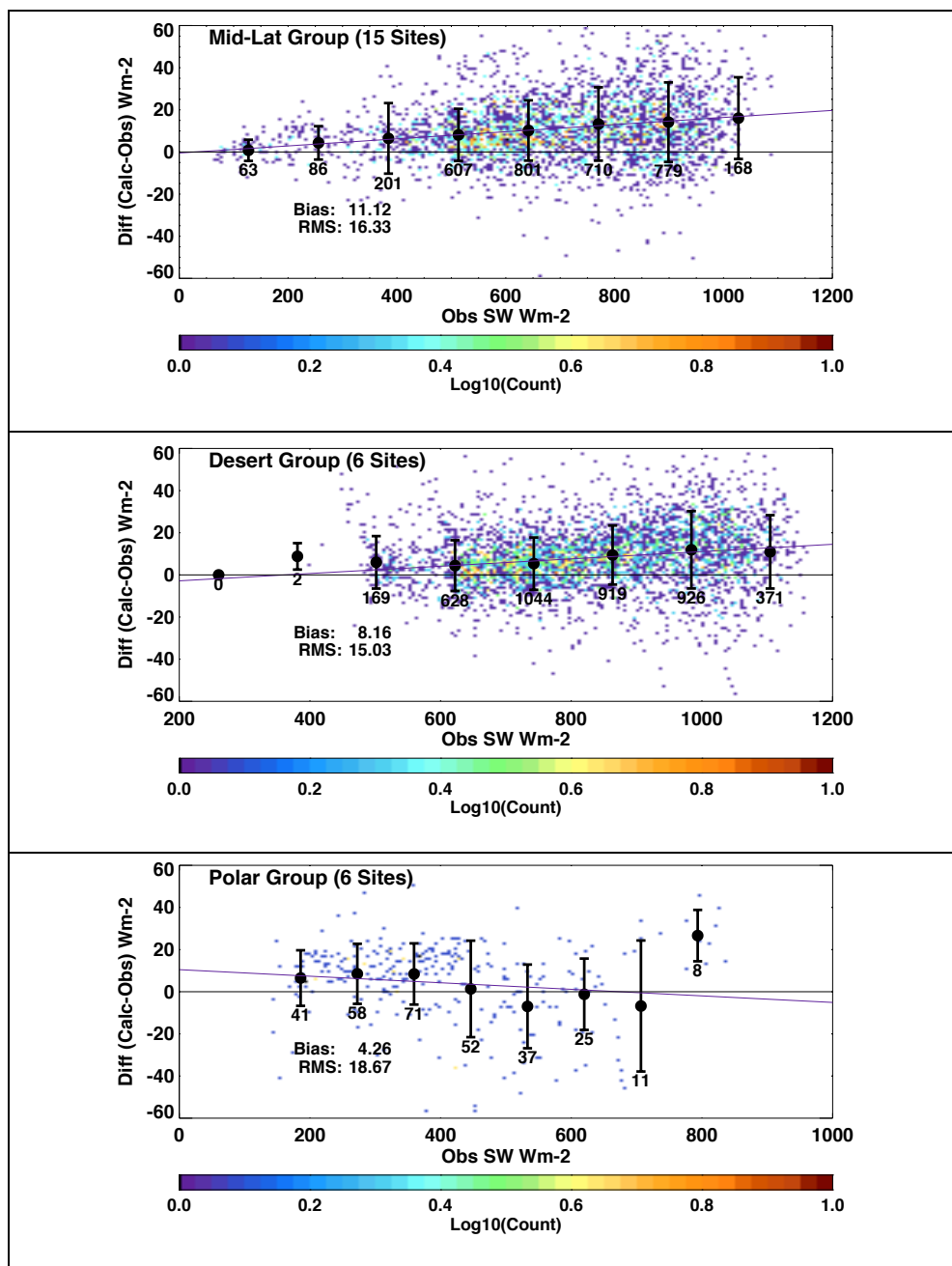


**Figure 13:** Difference of computed and observed clear-sky downward shortwave irradiance at the surface as a function of observed surface irradiances. Each data point is hourly mean irradiance. Clear-sky is identified by MODIS and ground based observations by the Long-Ackerman algorithm. Top, middle and bottom plots are for midlatitude, desert, and polar groups shown in Figure 11.



486 CERES instruments observe TOA irradiances, which can be used to assess the  
487 bias in computed irradiance. Global annual mean clear-sky TOA irradiances derived from  
488 CERES observation averaged over 20 years from March 2000 through February 2020 are  
489  $53 \text{ Wm}^{-2}$  for reflected shortwave irradiance and  $268 \text{ Wm}^{-2}$  for emitted longwave  
490 irradiance. Corresponding computed reflected shortwave flux is  $51 \text{ Wm}^{-2}$  and emitted  
491 longwave flux is  $267 \text{ Wm}^{-2}$ . Insight into the surface irradiance errors may be gained by  
492 considering how surface irradiance is modified via the tuning algorithm to match TOA  
493 irradiance in the CERES EBAF-surface product (Kato et al. 2018). To match the  
494 computed shortwave and longwave fluxes, AOD is increased from 0.136 to 0.156 (global  
495 annual mean values) and precipitable water is decreased from 2.29 cm to 2.22 cm (global  
496 annual mean values). These adjustments change the downward shortwave irradiance from  
497  $244 \text{ Wm}^{-2}$  to  $243 \text{ Wm}^{-2}$ .

498 To analyze how the EBAF tuning process changes surface irradiance, AOD and  
499 precipitable water, we computed the mean change separated by surface group shown in  
500 **Fig 12**. Generally, AOD increases and precipitable water decreases to increase reflected  
501 shortwave flux, which in turn decreases surface downward shortwave irradiance over  
502 these regions (**Table 3**). For the midlatitude group, on average, AOD is increased by  
503 0.02, precipitable water is decreased by 0.06 cm, and surface albedo is increased by 0.03.  
504 These adjustments reduce the diurnally averaged downward shortwave irradiance at the  
505 surface by  $2 \text{ Wm}^{-2}$ . We do not have exact matches of BSRN and AERONET surface sites  
506 but Tables 2 and 3 show MATCH AODs have either no bias (north America and China  
507 and south East Asia) or slightly negatively biased by 0.01 (Europe). Therefore, increasing  
508 MATCH AODs by 0.02 on average for the mid-latitude group seems justifiable.





509 However, decreasing  $2 \text{ Wm}^{-2}$  for the diurnally averaged downward shortwave is smaller  
510 than the  $12 \text{ Wm}^{-2}$  bias shown in the top right plot of **Fig. 10**, although instantaneous  
511 irradiances are used for **Fig. 10**. In addition, decreasing AODs for the desert group by  
512 0.02 contradicts the positive bias (0.07) for the North Africa group shown in Table 2  
513 under clear-sky conditions.

514 The adjustment made to match TOA shortwave irradiance, in the EBAF product,  
515 is within the uncertainty of MODIS-derived AOD of  $\pm 0.05$  over land and  $\pm 0.03$  over  
516 ocean (Remer et al. 2008; Levy et al. 2010, 2013). However, these are an expected error  
517 of instantaneous AOD retrieval derived from the comparison of AODs with AERONET.  
518 Therefore, the bias averaged over ground sites and many years is expected to be much  
519 smaller. Although, the 0.03 AOD adjustment over ocean might be the upper limit of the  
520 uncertainty of MODIS AODs over ocean,  $16 \text{ Wm}^{-2}$  bias in the instantaneous downward  
521 shortwave irradiance seems to be larger than the reduction by  $2 \text{ Wm}^{-2}$  in the diurnally  
522 averaged downward shortwave irradiance.

523 While we cannot identify the cause of the discrepancy between AOD comparison  
524 and downward shortwave irradiance comparison with surface observations, potential  
525 issues are following. 1) Aerosol type and optical properties used in irradiance  
526 computations, and 2) bias in downward shortwave irradiance measured by pyranometer,  
527 especially diffuse irradiance at smaller solar zenith angles. Because of the temperature  
528 gradient within pyranometer, the downward shortwave irradiance measured by a  
529 pyranometer tends to be biased low under clear-sky condition (Haeffelin et al. 2001).  
530 Note that a study by Ham et al. (2020) indicates that the bias of diurnally averaged



531 surface downward shortwave irradiance computed by a four-stream model should be  
532 smaller than 1%.

533

534 **Table 4:** Radiative flux, aerosol optical depth (AOD), precipitable water, and surface  
535 albedo change to match observed top-of-atmosphere radiative fluxes

	Changes: adjusted - unadjusted					
	Observed TOA upward shortwave irradiance ( $Wm^{-2}$ )	Clear-sky TOA upward shortwave irradiance ( $Wm^{-2}$ )	Clear-sky surface downward shortwave irradiance ( $Wm^{-2}$ )	Clear- sky AOD	Clear-sky precipitable water (cm)	Clear- sky surface albedo
Mid- latitude	63.3	3.9	-2.0	0.02	-0.06	0.03
Desert	92.3	3.4	-1.7	0.02	-0.04	0.01
Polar	86.5	8.2	-0.2	0.01	-0.03	0.10
Buoys	42.0	1.6	-2.0	0.03	-0.12	0.00

536

## 537 **5. Conclusions**

538 We evaluated MATCH aerosol optical depth used to produce the CERES  
539 SYN1deg product. Aerosol optical depths derived from Terra and Aqua by the dark target  
540 and deep blue algorithms were merged to produce daily gridded AODs. Daily gridded  
541 AODs were used for assimilation by MATCH at local solar noon. As a consequence,  
542 monthly mean AODs under clear-sky conditions identified by MODIS closely agree with  
543 those derived from MODIS, although MATCH uses climatological aerosol sources.  
544 Because AODs are not screened by QAC, MATCH AODs are larger over convective  
545 regions (e.g. Amazon, central Africa, and south east Asia) for both clear-sky and all-sky  
546 conditions.

547 MATCH AODs under all-sky conditions are larger than those under clear-sky  
548 conditions. Time series of AERONET AODs indicate that AODs generally increase with



549 cloud fraction, which is consistent with, primarily, water uptake by hygroscopic aerosols  
550 (Varnai et al, 2017). In addition, surface observations at the ARM SGP site suggest that a  
551 larger AODs and larger precipitable water under all-sky conditions than those under  
552 clear-sky conditions. Aerosol optical depth biases from AERONET AODs are  
553 comparable to biases of MERRA2 AOD biases from AERONET AODs for both all-sky  
554 and clear-sky conditions. However, MERRA2, which uses AERONET AODs to train the  
555 algorithm, has better temporal correlation with AERONET AODs than MATCH AODs.

556         Once MATCH AODs are used for surface irradiance computations, downward  
557 shortwave irradiances are positively biased by 1% to 2% compared to those observed at  
558 surface sites. Top-of-atmosphere reflected clear-sky shortwave irradiances are negatively  
559 biased compared with those derived from CERES observations. Increasing AODs by  
560  $\sim 0.02$ , and surface albedos by 0.03, and decreasing precipitable water by 0.06 cm over  
561 mid-latitude surface sites makes computed reflected TOA irradiances agree with those  
562 derived from CERES. These adjustments reduce downward shortwave irradiances at the  
563 surface by  $2 \text{ W m}^{-2}$ . Decreasing MATCH AODs for the desert group is needed to match  
564 computed reflected shortwave irradiances at TOA with those derived from CERES.  
565 However, decreasing MATCH AODs is not consistent with generally larger MATCH  
566 AODs compared with AERONET.

567         Although optical properties of aerosols (i.e. aerosol type) play a minor role in  
568 computing shortwave irradiance, changing aerosol type can alter the downward  
569 shortwave irradiance in the right direction. We did not investigate the error in aerosol  
570 type in this study. Aerosol types used in irradiance computations rely on those modeled  
571 by MATCH. Biases in the fraction of each aerosol type and their optical properties can



572 change TOA upward and surface downward shortwave irradiances without altering total  
573 AOD. Evaluation of aerosol type is left for the future study.

574

### 575 **Acknowledgments**

576 This work was funded by the NASA CERES project. The products and the  
577 validation could not have been accomplished without the help of the CERES TISA team.  
578 These data were obtained from the NASA Langley Research Center EOSDIS Distributed  
579 Active Archive Center. We also wish to acknowledge the hard work put in by the many  
580 dedicated scientists maintaining surface instrumentation in many diverse climates to  
581 obtain high quality observations of downwelling shortwave and longwave surface flux.  
582 Those groups are noted in Appendix A.

583

### 584 **Appendix A. Surface Observation Sites Used for Validation**

585 A great deal of data used in this study was collected by dedicated site scientists  
586 measuring critical climate variables around the world. The tables included in this  
587 appendix outline the sites, in situ measurements taken and their locations and dates of  
588 available data. Table A1 lists the locations of the AERONET sites, our source for  
589 observed aerosol optical depth which can be found on-line at:  
590 [https://aeronet.gsfc.nasa.gov/new\\_web/index.html](https://aeronet.gsfc.nasa.gov/new_web/index.html).

591

592

593

594



595

596

597

**Table A1. AERONET Observation Sites**

Region	Site	Location	Available Months
North Africa (6 Sites)	Saada, Morocco	31.6N, 8.2W	2004/07 - 2019/04
	Ouarzazate, Morocco	30.9N, 6.9W	2012/02 - 2015/06
	Tenerife Isl., Spain	28.3N, 16.5W	2004/07 - 2019/04
	Dhaka, Morocco	23.7N, 15.9W	2002/02 - 2005/11
	Tamanrasset, Algeria	22.8N, 8.2E	2004/07 - 2019/04
	Cape Verde Island	16.7N, 22.9W	2000/03 - 2018/12
Central Africa (5 Sites)	Ilorin, Nigeria	8.5N, 4.7E	2000/03 - 2019/09
	Koforidua, Ghana	6.1N, 0.3W	2012/12 - 2019/04
	Lope, Gabon	0.2S, 11.6E	2014/04 - 2018/02
	Mbita, Kenya	0.4S, 34.2E	2006/03 - 2017/17
	Bujumbura, Burundi	3.4S, 29.4E	2013/12 - 2019/04
China, Korea (8 Sites)	Xinglong, China	40.4N, 117.6E	2006/02 - 2014/11
	Beijing, China	39.9N, 116.4E	2001/03 - 2019/03
	Anyon Isl, S Korea	36.5N, 126.3E	2000/03 - 2019/11
	Yonsei Univ, S Korea	37.6N, 126.9E	2011/03 - 2019/01
	Cuiying Mt, China	35.9N, 104.1E	2006/07 - 2013/05
	Nanjing, China	32.2N, 118.7E	2008/03 - 2010/04
	Taihu, China	31.4N, 120.2E	2005/09 - 2016/08
	XiangHe, China	39.7N, 116.9E	2001/03 - 2017/05
India, SE Asia (8 Sites)	Gandhi College, India	25.8N, 84.1E	2006/04 - 2019/11
	Luang Namtha, Laos	20.9N, 101.4E	2001/04 - 2019/02
	Omkoj, Thailand	17.8N, 98.4E	2003/02 - 2018/03
	Dhaka Univ, Bangladesh	23.7N, 90.3E	2012/06 - 2019/07
	Bhola, Bangladesh	22.2N, 90.7E	2013/04 - 2019/04
	Nghia Do, Vietnam	21.0N, 105.8E	2010/11 - 2019/09
	Pune, India	18.5N, 73.8E	2004/10 - 2019/06
	Hanimaadhoo, Maldives	6.7N, 73.2E	2004/11 - 2019/09

598

599

600

601

602

603

604

605

606

607

608

609

610



611  
 612  
 613  
 614

Table A1. AERONET Observation Sites (Continued)

Region	Site	Location	Available Months
Brazil (7 Sites)	Petrolina, Brazil	9.1S, 40.4W	2004/07 - 2016/11
	Abracos Hill, Brazil	10.7S, 62.4W	2000/03 - 2005/10
	Alta Floresta, Brazil	9.9S, 56.1W	2000/05 - 2019/02
	Belterra, Brazil	2.6S, 55.0W	2000/03 - 2005/04
	Ji Parana SE, Brazil	10.9S, 61.9W	2006/01 - 2017/10
	Manaus, Brazil	2.9S, 60.0W	2011/02 - 2019/05
	Rio Branco, Brazil	9.9S, 67.9W	2000/07 - 2017/10
Australia (6 Sites)	Jabiru, Australia	12.6S, 132.9E	2000/03 - 2019/09
	Lake Argyle, Australia	16.1S, 128.7E	2001/10 - 2019/09
	Canberra, Australia	35.3S, 149.1E	2003/01 - 2017/08
	Birdsville, Australia	25.9S, 139.3E	2005/08 - 2018/06
	Lucinda, Australia	18.5S, 146.4E	2009/10 - 2020/01
	Lake Lefroy, Australia	31.2S, 121.7E	2012/06 - 2019/12
North America (10 Sites)	Brats Lake, Canada	50.2N, 104.7W	2000/03 - 2013/02
	Sioux Falls, SD	43.7N, 96.6W	2001/06 - 2017/10
	Ames, IA	42.0N, 93.8W	2004/05 - 2019/03
	Boulder Tower	40.0N, 105W	2001/05 - 2016/07
	Bondville, IL	40.0N, 88.4W	2000/03 - 2017/10
	Brookhaven, NY	40.8N, 72.9W	2002/09 - 2020/01
	Wallops Island, VA	37.9N, 75.5W	2003/03 - 2020/03
	ARM/SGP E13	36.6N, 97.5W	2000/03 - 2018/05
	Chesapeake Light Tower	36.9N, 75.7W	2000/03 - 2016/01
	Table Mountain, CO	40.1N, 105.2W	2008/11 - 2017/12
Europe (10 Sites)	Cabauw, Netherlands	51.9N, 4.9E	2003/04 - 2017/11
	Palaiseau, France	48.7N, 2.2E	2000/03 - 2020/10
	Torevere, Estonia	58.2N, 26.5E	2002/06 - 2019/07
	Kishinev, Moldova	47.0N, 28.8E	2000/03 - 2018/11
	Belsk, Poland	51.8N, 20.8E	2004/01 - 2016/08
	Kyiv, Ukraine	50.3N, 30.5E	2007/04 - 2018/12
	Hamburg, Germany	53.5N, 9.9E	2000/06 - 2018/06
	Munich Univ, Germany	48.1N, 11.6E	2001/11 - 2019/05
	Thessaloniki, Greece	40.6N, 22.1E	2003/06 - 2020/03
	Bucharest, Hungary	44.3N, 26.0E	2000/10 - 2019/03

615

616 Sources of surface observed downwelling irradiance are outlined in Tables  
 617 A2 (land) and A3 (buoys). For land we utilize data from the Baseline Surface  
 618 Radiation Network (BSRN) (Dreimel et al, 2018; Ohmura et al. (1998)), the US Dept.  
 619 of Energy's Atmospheric Radiation Measurement (ARM) program and NOAA's  
 620 SURFRAD network available from NOAA's Air Resources Laboratory/Surface  
 621 Radiation Research Branch., Augustine et al. (2000). Buoy observations come from



622 two sources through four separate projects. The Upper Ocean Processes group at  
623 Woods Hole Oceanographic Institute have maintained the Stratus, North Tropical  
624 Atlantic Site (NTAS) and Hawaii Ocean Time Series (HOTS) buoys for more than a  
625 decade providing valuable time series of radiation observations in climatically  
626 important regions of the ocean. These data can be retrieved from:  
627 <http://uop.whoi.edu/index.html>. We would also like to acknowledge the Project  
628 Office of NOAA's Pacific Marine Environmental Labs (PMEL) where three groups of  
629 buoy data were downloaded: In the Pacific, the Tropical Atmosphere  
630 Ocean/Triangle Trans-Ocean Buoy Network (TAO/TRITON) (McPhaden, 2002) data,  
631 from the tropical Atlantic Ocean, the Prediction and Research Moored Array in the  
632 Tropical Atlantic (PIRATA) (Servain et al. 1998), and the Research Moored Array for  
633 African - Asian - Australian Monsoon Analysis and Prediction (RAMA) (McPhaden et  
634 al., 2009) in the Indian Ocean. Also downloaded from PMEL are the long-term buoy  
635 observations PAPA and Kuroshio Current observatory sites.

636

637

638

639

640

641

642

643

644



Table A2. Surface Irradiance Validation Sites (Land)

Region	Site	Location	Source
Mid-Latitude (15 Sites)	Lindenberg, Germany	52.2N, 14.1E	BSRN
	Cabauw, Netherlands	51.9N, 4.9E	BSRN
	Fort Peck, MT	48.3N, 105.1W	BSRN
	Payerne, Switzerland	46.8N, 6.9E	BSRN
	Penn State, PA	40.7N, 77.9W	SURFRAD
	Beijing, China	39.9N, 116.3E	BSRN
	E13, Lamont, OK	36.6N, 97.5W	ARM
	Ches Light Tower, USA	36.9N, 75.7W	BSRN
	Tateno, Japan	36.1N, 140.1E	BSRN
	Goodwin Creek, MS	34.2N, 89.9W	SURFRAD
	De Aar, South Africa	30.6S, 24.0E	BSRN
	Lauder, New Zealand	45.0S, 169.7E	BSRN
	Florianapolis, Brazil	27.5S, 48.5W	BSRN
	Brasilia, Brazil	15.6S, 47.7W	BSRN
	Sao Martinho da Serra, Brazil	29.4S, 53.8W	BSRN
Desert (6 Sites)	Sede Boqer, Israel	30.8N, 34.7E	BSRN
	Saudi Solar Village	24.9N, 46.4E	BSRN
	Tamanrasset, Algeria	22.8N, 5.5E	BSRN
	Desert Rock, NV	36.6N, 116.1W	SURFRAD
	Alice Springs, Australia	23.7S, 133.8E	BSRN
	Gobabeb, Namibia	23.5S, 15.0E	BSRN
Polar (6 Sites)	Alert, Canada	82.5N, 62.4W	BSRN
	Tiksi, Russia	71.6N, 128.9E	BSRN
	Barrow, Alaska	71.3N, 156.7W	BSRN
	Syowa, Antarctica	69.0S, 39.5E	BSRN
	South Pole, Antarctica	90.0S, 0.5E	BSRN
	G. von Neumayer, Antarctica	-70.6S, 8.3W	BSRN

645  
 646  
 647  
 648

BSRN: Baseline Surface Radiation Network, <http://bsrn.awi.de/>  
 SURFRAD: NOAA- SURFace RADiation Program, <http://www.esrl.noaa.gov/gmd/grad/surfrad/>  
 ARM: US Dept of Energy, Atmospheric Radiation Measurement Program, <http://www.arm.gov/>

Table A3. Surface Observation Sites for Ocean Buoy Locations

Program Name	Data Source	Locations
Upper Ocean Processes Group (UOP) 3 Buoys	Woods Hole Oceanographic Institute	Stratus Buoy -20.2N, 85.0W
		North Tropical Atlantic Buoy 14.5N, 51.0W
		Hawaii Ocean Time Series Buoy 22.5N, 158W
PIRATA Buoys 14 Buoys	Pacific Marine Environmental Laboratory (PMEL)	East Atlantic Ocean
RAMA Buoys 10 Buoys	PMEL	Tropical Indian Ocean
TAO Array Buoys 17 Buoys	PMEL	E & W Tropical Pacific Ocean
Kuroshio Extension Observatory Buoy	PMEL	NW Pacific, 32.4N, 144.6E
PAPA Sub-Arctic Ocean Buoy	PMEL	NE Pacific, 50.1N, 144.8W

649  
 650  
 651

UOP: <http://uop.whoi.edu/projects/projects.htm>  
 PMEL: [http://www.pmel.noaa.gov/tao/data\\_deliv/deliv.html](http://www.pmel.noaa.gov/tao/data_deliv/deliv.html)

652





653 **References**

- 654 Augustine, J. A., DeLuisi, J. J., and Long, C. N.: SURFRAD – A national surface radiation  
655 budget network for atmospheric research, *Bull. of Amer. Met. Soc.* 81, No. 10, pp.  
656 2341-2358, 2000.
- 657 Barth, M. C., Rasch, P. J., Kiehl, J. T., Benkovitz, C. M., and Schwartz, S. E.: Sulfur  
658 chemistry in the NCAR CCM: Description, evaluation, features and sensitivity to  
659 aqueous chemistry, *J. Geophys. Res.*, 106, 20 311–20 322, 2000.
- 660 Bauer, S. E. and Menon, S.: Aerosol direct, indirect, semidirect, and surface albedo  
661 effects from sector contributions based on the IPCC AR5 emissions for  
662 preindustrial and present-day conditions, *J. Geophys. Res.*, 117, D01206,  
663 doi:10.1029/2011JD016816, 2012.
- 664 Benkovitz, C. M., Scholtz, M. T., Pacyna, J., Tarrason, L., Dignon, J., Voldner, E. C., Spiro,  
665 P. A., Logan, J. A., and Graedel, T. E.: Global gridded inventories of anthropogenic  
666 emissions of sulfur and nitrogen, *J. Geophys. Res.: Atmos.* 101 (D22), 29,239–  
667 29,253, 1996.
- 668 Blanchard, D. C. and Woodcock, A. H.: The production, concentration and vertical  
669 distribution of the sea-salt aerosol, *Ann. Of the NY Acad. Of Sci.*,  
670 doi:10.1111/j.1749-6632.1980.tb17130, 1980.
- 671 Boucher, O., Randall, D., Artaxo, P., Bretherton, C., Feingold, G., Forster, P., Kerminen,  
672 V.-M., Kondo, Y., Liao, H., Lohmann, U., Rasch, P., Satheesh, S.K., Sherwood, S.,  
673 Stevens, B. and Zhang, X. Y.: Clouds and Aerosols. In: *Climate Change 2013: The*  
674 *Physical Science Basis. Contribution of Working Group I to the Fifth Assessment*  
675 *Report of the Intergovernmental Panel on Climate Change* [Stocker, T.F., D. Qin,



- 676 G.-K. Plattner, M. Tignor, S.K. Allen, J. Boschung, A. Nauels, Y. Xia, V. Bex and P.M.  
677 Midgley (eds.)]. Chapter 7. Cambridge University Press, Cambridge, United  
678 Kingdom and New York, NY, U, 2013.
- 679 Colbo, K. and Weller, R. A.: Accuracy of the IMET sensor package in the subtropics. J.  
680 Atmos. Oceanic Technol., 26, 1867–1890,  
681 <https://doi.org/10.1175/2009JTECHO667.1>, 2009.
- 682 Collins, W. D., Rasch, P. J., Eaton, B. E., B. Khattatov, V., Lamarque, J-F. and Zender, C.  
683 S.: Simulating aerosols using a chemical transport model with assimilation of  
684 satellite aerosol retrievals: Methodology for INDOEX. J. Geophys. Res., 106 (D7),  
685 7313–7336, 2001.
- 686 Driemel, A., and Co-authors: Baseline Surface Radiation Network (BSRN): structure and  
687 data description (1992–2017), Earth Syst. Sci. Data, 10, 1491-1501,  
688 [doi:10.5194/essd-10-1491-2018](https://doi.org/10.5194/essd-10-1491-2018). 2018
- 689 Emmons, L. K., and co-authors: Description and evaluation of the Model for Ozone and  
690 Related chemical Tracers, version 4 (MOZART-4), Geosci. Model Dev., 3, 43–67.  
691 [www.geosci-model-dev.net/3/43/2010/](http://www.geosci-model-dev.net/3/43/2010/), 2010.
- 692 Fu, Q. and Liou, K-N.: Parameterization of the radiative properties of cirrus clouds, J.  
693 Atmos. Sci., 50, 2008–2025, 1993.
- 694 Fu, Q., Lesins, G., Higgins, J., Charlock, T., Chylek, P. and Michalsky, J.: Broadband  
695 water vapor absorption of solar radiation tested using ARM data. Geophys. Res. Let.,  
696 25, 1169–1172, 1998.



- 697 Ginoux, P., Chin, M., Tegen, I., Prospero, J. M., Holben, B., Dubovik, O. and Lin, S-J.:  
698 Sources and distributions of dust aerosols simulated with the GOCART model J. of  
699 Geophys. Res.: Atmos., 106, 20255-20273, doi.org/10.1029/2000JD000053, 2001.
- 700 Haeffelin, M., Kato, S., Smith, A. M., Rutledge, C. K., Charlock T. P. and Mahan, J. R.:  
701 Determination of the thermal offset of the Eppley precision spectral pyranometer,  
702 Appl. Opt. 40, 472-484, 2001.
- 703 Ham, S., Kato, S. and Rose, F. G.: Examining biases in diurnally-integrated shortwave  
704 irradiances due to two- and four-stream approximations in cloudy atmosphere. J.  
705 Atmos. Sci., 77(2), 551–581. doi: 10.1175/JAS-D-19-0215.1, 2020.
- 706 Hess, M., Koepke, P. and Schult, I.: Optical Properties of Aerosols and Clouds: The  
707 software package OPAC. Bull. Amer. Meteor. Soc., 79, 831-844.  
708 [https://doi.org/10.1175/1520-0477\(1998\)079<0831:OPOAAC>2.0.CO;2](https://doi.org/10.1175/1520-0477(1998)079<0831:OPOAAC>2.0.CO;2), 1998.
- 709 Holben B.N., Eck, T. F., Slutsker, I., Tanre, D., Buis, J. P., Setzer, A., Vermote, E.,  
710 Reagan, J. A., Kaufman, Y., Nakajima, T., Lavenu, F., Jankowiak, I. and Smirnov,  
711 A.: AERONET - A federated instrument network and data archive for aerosol  
712 characterization, Rem. Sens. Environ., 66, 1-16, 1998
- 713 Hsu, N. C., Tsay, S-C, King, M. D. and Herman, J. R.: Deep Blue Retrievals of Asian  
714 Aerosol Properties During ACE-Asia, IEEE Trans. On Geosci. and Rem. Sens.,  
715 44(11), 2006.
- 716 Huneeus, N., and co-authors: Global dust model intercomparison in AeroCom phase I,  
717 Atmos. Chem. Phys., 11, 7781–7816. [www.atmos-chem-phys.net/11/7781/2011/](http://www.atmos-chem-phys.net/11/7781/2011/)  
718 doi:10.5194/acp-11-7781-2011, 2011.



- 719 Kato, S., Loeb, N. G., Rose, F. G., Doelling, D. R., Rutan, D. A., Caldwell, T. E., Yu L.  
720 and Weller, R. A.: Surface irradiances consistent with CERES-derived top-of-  
721 atmosphere shortwave and longwave irradiances. *J. of Clim Dyn.* doi: 10.1175/JCLI-  
722 D-12-00436, 2013.
- 723 Kato, S., Rose, F. G., Rutan, D. A., Thorsen, T. J., Loeb, N. G., Doelling, D. R., Huang,  
724 X., Smith, W. L., Su, W. and Ham, S-H.: Surface Irradiances of Edition 4.0 Clouds  
725 and the Earth's Radiant Energy System (CERES) Energy Balanced and Filled  
726 (EBAF) Data Product. *J. of Clim Dyn.* doi: 10.1175/JCLI-D-17-0523.1, 2018.
- 727 Kaufman, Y. and co-authors: A critical examination of the residual cloud contamination  
728 and diurnal sampling effects on MODIS estimates of aerosol over ocean, *IEEE Trans.*  
729 *Geosci. Rem. Sens.* 43, DOI: 10.1109/TGRS.2005.858430, 2005.
- 730 Kinne, S. and co-authors: An AeroCom initial assessment – optical properties in aerosol  
731 component modules of global models. *Atmos. Chem. Phys.*, 6, 1815–1834.  
732 [www.atmos-chem-phys.net/6/1815/2006/](http://www.atmos-chem-phys.net/6/1815/2006/), 2006.
- 733 Koch, D., and co-authors: Evaluation of black carbon estimations in global aerosol  
734 models. *Atmos. Chem. Phys.*, 9, 9001–9026. [www.atmos-chem-](http://www.atmos-chem-phys.net/9/9001/2009/)  
735 [phys.net/9/9001/2009/](http://www.atmos-chem-phys.net/9/9001/2009/), 2009.
- 736 L'Ecuyer T. S., Beaudoin, H. K., Rodell, M., Olson, W., Lin, B., Kato, S., Clayson, C.  
737 A., Wood, E., Sheffield, J., Adler, R., Huffman, G., Bosilovich, M., Gu, G.,  
738 Robertson, F., Houser, P. R., Chambers, D., Famiglietti, J. S., Fetzer, E., Liu, W. T.,  
739 Gao, X., Schlosser, C. A., Clark, E., Lettenmaier, D. P. and Hilburn, K.: The  
740 observed state of the energy budget in the early twenty-first century. *J Clim*  
741 28(21):8319–8346. <https://doi.org/10.1175/Jcli-D-14-00556.1>, 2015.



- 742 Levy, R. C., Remer, L. A., Kleidman, R. G., Mattoo, S., Ichoku, C., Kahn R. and Eck, T.  
743 F.: Global evaluation of the collection 5 MODIS dark-target aerosol products over  
744 land. *Atmos. Chem and Phys.*, 10, 103999-10420. [https://doi.org/10.5194/acp-10-](https://doi.org/10.5194/acp-10-10399-2010)  
745 10399-2010, 2010.
- 746 Levy, R. C., Mattoo, S., Munchak, L. A., Remer, L. A., Sayer, A. M., Patadia, F. and  
747 Hsu, N. C.: The Collection 6 MODIS aerosol products over land and ocean. *Atmos.*  
748 *Meas. Tech.*, 6, 2989-3034, 10.5194/amt-6-2989-2013, 2013.
- 749 Liousse, C., Penner, J. E., Chuang, C., Walton, J. J., Eddleman, H. and Cachier, H.: A  
750 global three-dimensional model study of carbonaceous aerosols, *J. Geophys. Res. A.*,  
751 101(D14), 19 411– 19 432, 1996.
- 752 Loeb, N. G., Kato, S., Loukachine, K. and Smith, N. M.: Angular Distribution Models for  
753 Top-of-Atmosphere Radiative Flux Estimation from the Clouds and the Earth's  
754 Radiant Energy System Instrument on the Terra Satellite. Part I: Methodology, *J.*  
755 *Atmos. Oceanic Technol*, 22, 338-351, 2005.
- 756 Loeb, N. G. and Su, W.: Direct Aerosol Radiative Forcing Uncertainty Based on a  
757 Radiative Perturbation Analysis. *J. Climate*, 23(19), 5288-5293. doi:  
758 10.1175/2010JCLI3543.1, 2010.
- 759 Loeb, N. G., Doelling, D. R., Wang, H., Su, W., Nguyen, C., Corbett, J. G., Liang, L., Mitrescu,  
760 C., Rose, F. G. and Kato, S.: Clouds and the Earth's Radiant Energy System (CERES)  
761 Energy Balanced and Filled (EBAF) top-of-atmosphere (TOA) Edition-4.0 data  
762 product. *J. Climate*, 31, 895–918, <https://doi.org/10.1175/JCLI-D-17-0208.1>,  
763 2018.



- 764 Long, C. N., Ackerman, T. P., Gaustad, K. L. and Cole, J. N. S.: Estimation of fractional  
765 sky cover from broadband shortwave radiometer measurements, *J. Geophys.*  
766 *Res.*,111, D11204, doi:10.1029/2005JD006475, 2006.
- 767 Martins, J. V., D. Tanre, D., Remer, L., Kaufman, Y., Mattoo, S. and Levy, R.: MODIS cloud  
768 screening for remote sensing of aerosols over oceans using spatial variability,  
769 *Geophys. Res. Lett.*, 29, 1619, DOI:10.1029/2001GL013252, 2002.
- 770 McPhaden, M. J.: TAO/TRITON tracks Pacific Ocean warming in early 2002. CLIVAR  
771 Exchanges, No. 24, International CLIVAR Project Office, Southampton, United  
772 Kingdom, 7–9, 2002.
- 773 #——, and Coauthors: RAMA: The Research Moored Array for African–Asian–  
774 Australian Monsoon Analysis and Pre- diction. *Bull. Amer. Meteor. Soc.*, 90, 459–  
775 480, doi:10.1175/ 2008BAMS2608.1, 2009.
- 776 Michalsky, J. J., Gueymard, C., Kiedron, P., McArthur, L. J. B., Philipona, R. and  
777 Stoffel, T.: A proposed working standard for the measurement of diffuse horizontal  
778 shortwave irradiance. *J. of Geophys. Res. A.*, 112(D16),  
779 <https://doi.org/10.1029/2007JD008651>, 2007.
- 780  
781 Minnis, P., Sun-Mack, S., Chen, Y., Chang, F., Yost, C. R., Smith, W. L., Heck, P. W.,  
782 Arduini, R. F., Bedka, S. T., Yi, Y., Hong, G., Jin, Z., Painemal, D., Palikonda, R.,  
783 Scarino, B. R., Spangenberg, D. A., Smith, R. A., Trepte, Q. Z., Yang, P. and Xie, Y.:  
784 CERES MODIS Cloud Product Retrievals for Edition 4–Part I: Algorithm Changes.  
785 *IEEE Transactions on Geoscience and Remote Sensing*, 1–37. doi:  
786 10.1109/TGRS.2020.3008866, 2020.
- 787 Ohmura A., Dutton, E., Forgan, B., Frohlich, C., Gilgen, H., Hegne, H., Heimo, A., Konig-



- 788 Langlo, G., McArthur, B., Muller, G., Philipona, R., Whitlock, C., Dehne, K. and Wild,  
789 M.: Baseline Surface Radiation Network (BSRN/WCRP): New precision  
790 radiometry for climate change research. *Bull. Amer. Meteor. Soc.*, 79, No. 10,  
791 2115-2136, 1998.
- 792 Randles, C. A., Da Silva, A. M., Buchard, V., Colarco, P. R., Darmenov, A., Govindaraju,  
793 R., Smirnov, A., Holben, A., Ferrare, R., Hair, J., Shinozuka, Y. and Flynn, C. J.: The  
794 MERRA-2 aerosol reanalysis, 1980 onward. Part I: System description and data  
795 assimilation evaluation, *J. Clim.* 30(17), [http://dx.doi.org/10.1175/JCLI-D-16-](http://dx.doi.org/10.1175/JCLI-D-16-0609.s1)  
796 0609.s1, 2017.
- 797 Rasch, P. J., Mahowald, N. M. and Eaton, B. E.: Representations of transport,  
798 convection, and the hydrologic cycle in chemical transport models: Implications  
799 for the modeling of short-lived and soluble species. *J. of Geo. Res.*, 102, 127-138,  
800 1997.
- 801 Rasch, P. J., Collins, W. D. and Eaton, B. E.: Understanding the Indian Ocean  
802 Experiment (INDOEX) aerosol distributions with an aerosol assimilation. *J. of*  
803 *Geo. Res.*, 106, 7337-7355, 2001.
- 804 Remer, L. A., and Co-authors: The MODIS aerosol algorithm, products, and validation. *J.*  
805 *Atmos. Sci.*, 62, 947–973, 2005.
- 806 Remer, L. A., Kleidman, R. G., Levy, R. C., Kaufman, Y. J., Tanre, D., Mattoo, S.,  
807 Vanderlei Martins, J., Ichoku, C., Koren, I., Yu, H. and Holben, B. N.: Global aerosol  
808 climatology from the MODIS satellite sensors. *J. Geophys. Res.: A.* 113(D14),  
809 <https://doi.org/10.1029/2007JD009661>, 2008.
- 810 Rose, F. G., Rutan, D. A., Charlock, T., Smith, G. L. and Kato, S.: An Algorithm for the



811        Constraining of Radiative Transfer Calculations to CERES-Observed Broadband  
812        Top-of-Atmosphere Irradiance. *J. Atmos. and Ocean. Tech.* 30, 1091-1106. DOI:  
813        10.1175/JTECH-D-12-00058.1, 2013.

814    Rutan, D., Rose, F., Roman, M., Manalo-Smith, N., Schaaf, C. and Charlock, T.:  
815        Development and assessment of broadband surface albedo from Clouds and the  
816        Earth's Radiant Energy System clouds and radiation swath data product. *J. Geophys.*  
817        *Res.*, 114, D08125. doi:10.1029/2008JD010669, 2009.

818    Rutan, D., Kato, S., Doelling, D. R., Rose, F. G., Nguyen, L. T. and Caldwell, T.: CERES  
819        Synoptic Product: Methodology and Validation of Surface Radiant Flux. *J. Atmos.*  
820        *And Ocean. Tech.*, 32, doi:10.1175/JTECH-D-14-00165.1, 2015.

821    Servain, J., Busalacchi, A. J., McPhaden, M. J., Moura, A. D., Reverdin, G., Vianna, M.  
822        and Zebiak, S. E.: A Pilot Research Moored Array in the Tropical Atlantic  
823        (PIRATA). *Bull. Amer. Meteor. Soc.*, 79, 2019–2031, doi:10.1175/1520-  
824        0477(1998)079,2019:APRMAI.2.0.CO;2. 1998

825    Sinyuk, A., Torres, O. and Dubovik, O.: Combined use of satellite and surface  
826        observations to infer the imaginary part of refractive index of Saharan dust.  
827        *Geophysical Research Letters*, 30(2), 1081. <https://doi.org/10.1029/2002GL016189>,  
828        2003.

829    Smirnov, A., Holben, B. N., Eck, T. F., Dubovik, O. and Slutsker, I.: Cloud-screening  
830        and quality control algorithms for the AERONET database. *Rem. Sens. Env.* 73, 337-  
831        349, 2000.

832    Soden, B. and Chung, E-S.: The Large-Scale Dynamical Response of Clouds to Aerosol  
833        Forcing. *J. of Climate*, 30, 8783-8794. doi: <https://doi.org/10.1175/JCLI-D-17->





- 834 [0050.1](#), 2017.
- 835 Stephens, G. L., Slingo, J. M., Rignot, E., Reager, J. T., Hakuba, M. Z., Durack, P. J.,  
836 Worden, J. and Rocca, R.: Earth's water reservoirs in a changing climate. Proc. R.  
837 Soc. A 476: 20190458. <http://dx.doi.org/10.1098/rspa.2019.0458>, 2020.
- 838 Su, W., Schuster, G. L., Loeb, N. G., Rogers, R. R., Ferrare, R. A., Hostetler, C. A., Hair,  
839 J. W., and Obland, M. D.: Aerosol and cloud interaction observed from high spectral  
840 resolution lidar data. J. of Geophys. Res.: Atmos., 113(D24), D24202.  
841 Doi:10.1029/2008JD010588, 2008.
- 842 Su, W., Corbett, J., Eitzen, Z. and Liang, L.: Next-generation angular distribution models  
843 for top-of-atmosphere radiative flux calculation from CERES instruments:  
844 methodology. Atmos. Meas. Tech., 8(2), 611-632. doi: 10.5194/amt-8-611-2015,  
845 2015.
- 846 Su, W., Corbett, J., Eitzen, Z. and Liang, L.: Next-generation angular distribution models  
847 for top-of-atmosphere radiative flux calculation from CERES instruments: validation.  
848 Atmos. Meas. Tech., 8(8), 3297-3313. doi: 10.5194/amt-8-3297-2015, 2015.
- 849 Su, W., G. L. Schuster, N. G. Loeb, R. R. Rogers, R. A. Ferrare, C. A. Hostetler, J. W.  
850 Hair, M. D. Obland, 2008: Aerosol and cloud interaction observed from high spectral  
851 resolution lidar data. J. of Geophys. Res.: Atmos., 113(D24), D24202.  
852 Doi:10.1029/2008JD010588.
- 853 Textor, C. and Co-authors: Analysis and quantification of the diversities of aerosol  
854 life cycles within AeroCom, Atmos. Chem. Phys., 6, 1777-1813. [www.atmos-](http://www.atmos-chem-phys.net/6/1777/2006/)  
855 [chem-phys.net/6/1777/2006/](http://www.atmos-chem-phys.net/6/1777/2006/), 2006.
- 856 Textor, C., and Co-authors: The effect of harmonized emissions on aerosol



857 properties in global models – an AeroCom experiment. *Atmos. Chem. Phys.*, 7,  
858 4489–4501. [www.atmos-chem-phys.net/7/4489/2007/](http://www.atmos-chem-phys.net/7/4489/2007/), 2007.

859 Varnai, T., Marshak, A. and Eck, T. F.: Observation-based study on aerosol optical depth  
860 and particle size in partly cloudy regions. *J. Geophys. Res. A*. 122, 10,013–10,024,  
861 <https://doi.org/10.1002/2017JD027028>, 2017.

862 Wen, G., Marshak, A., Cahalan, R. F., Remer, L. A. and Kleidman, R. G.: 3-D aerosol-  
863 cloud radiative interaction observed in collocated MODIS and ASTER images of  
864 cumulus cloud fields, *J. Geophys. Res.*, 112, D13204, doi:10.1029/2006JD008267,  
865 2007.

866 Wielicki, B. A., Barkstrom, B. R., Harrison, E. F., Lee, R. B. III, Smith, G. L. and Cooper, J.  
867 E.: Clouds and the Earth's Radiant Energy System (CERES): An Earth Observing  
868 System Experiment. *Bull. Amer. Meteor. Soc.*, 77, 853-868, 1996.

869 Zender, C. S., Huishen, B. and Newman, D.: Mineral Dust Entrainment and Deposition  
870 (DEAD) model: Description and 1990s dust climatology. *J. Geophys. Res.*, 108,  
871 doi:10.1029/2002JD002775, 2003.